DEVELOPING METHODS BASED ON LIGHT SHEET FLUORESCENCE MICROSCOPY FOR BIOPHYSICAL INVESTIGATIONS OF LARVAL ZEBRAFISH

by

MICHAEL J. TAORMINA

A DISSERTATION

Presented to the Department of Physics
and the Graduate School of the University of Oregon
in partial fulfillment of the requirements
for the degree of
Doctor of Philosophy

June 2014

DISSERTATION APPROVAL PAGE

Student: Michael J. Taormina

Title: Developing Methods Based on Light Sheet Fluorescence Microscopy for Biophysical Investigations of Larval Zebrafish

This dissertation has been accepted and approved in partial fulfillment of the requirements for the Doctor of Philosophy degree in the Department of Physics by:

Gregory Bothun	Chair
Raghuveer Parthasarathy	Advisor
Eric Corwin	Core Member
Karen Guillemin	Institutional Representative

and

Kimberly Andrews Espy	Vice President for Research & Innovation/ Dean of the Graduate School

Original approval signatures are on file with the University of Oregon Graduate School.

Degree awarded June 2014

DISSERTATION ABSTRACT

Michael J. Taormina

Doctor of Philosophy

Department of Physics

June 2014

Title: Developing Methods Based on Light Sheet Fluorescence Microscopy for Biophysical Investigations of Larval Zebrafish

Adapting the tools of optical microscopy to the large-scale dynamic systems encountered in the development of multicellular organisms provides a path toward understanding the physical processes necessary for complex life to form and function. Obtaining quantitatively meaningful results from such systems has been challenging due to difficulty spanning the spatial and temporal scales representative of the whole, while also observing the many individual members from which complex and collective behavior emerges.

A three-dimensional imaging technique known as light sheet fluorescence microscopy provides a number of significant benefits for surmounting these challenges and studying developmental systems. A thin plane of fluorescence excitation light is produced such that it coincides with the focal plane of an imaging system, providing rapid acquisition of optically sectioned images that can be used to construct a three-dimensional rendition of a sample. I discuss the implementation of this technique for use in larva of the model vertebrate *Danio rerio* (zebrafish).

The nature of light sheet imaging makes it especially well suited to the study of large systems while maintaining good spatial resolution and minimizing damage to the specimen from excessive exposure to excitation light. I show the results from a comparative study that demonstrates the ability to image certain developmental processes non-destructively, while in contrast confocal microscopy results in abnormal growth due to phototoxicity. I develop the application of light sheet microscopy to the study of a previously inaccessible system: the bacterial colonization of a host organism. Using the technique, we are able to obtain a survey of the intestinal tract of a larval zebrafish and observe the location of microbes as they grow and establish a stable population in an initially germ free fish. Finally, I describe a new technique to measure the fluid viscosity of this intestinal environment *in vivo* using magnetically driven particles. By imaging such particles as they are oscillated in a frequency chirped field, it is possible to calculate properties such as the viscosity of the material in which they are embedded. Here I provide the first known measurement of intestinal mucus rheology *in vivo*.

This dissertation includes previously published co-authored material.

CURRICULUM VITAE

NAME OF AUTHOR: Michael J. Taormina

GRADUATE AND UNDERGRADUATE SCHOOLS ATTENDED:

University of Oregon, Eugene
Colorado State University, Fort Collins

DEGREES AWARDED:

Doctor of Philosophy in Physics, University of Oregon (2014).
Master of Science, University of Oregon (2009).
Bachelor of Science in Physics, Clark Honors College, University of Oregon (2006).

AREAS OF SPECIAL INTEREST:

Advanced microscopy techniques, especially for use in multicellular biological and biophysical systems of study. Computational image processing and machine vision.

PROFESSIONAL EXPERIENCE:

Graduate Research Assistant, Department of Physics, University of Oregon, Eugene, OR (2009-2014).

Summer school participant, Center for the Physics of Living Cells (U. Illinois, Urbana-Champaign) (2010).
Project title: *Tracking Cell Surface Growth in Living Fruit Fly Embryos.*
Principle investigator: Anna Sokac, Baylor College of Medicine.

Graduate Teaching Fellow, Department of Physics, University of Oregon, Eugene, OR (2008-2009).

Graduate Teaching Assistant, Department of Physics, Colorado State University, Fort Collins, CO (2007-2008).

Student Research Assistant, University of Oregon, Eugene, OR (2004-2006)

GRANTS, AWARDS AND HONORS:

National Science Foundation GK12 Fellowship in K-5 STEM education (2010-2012).

PUBLICATIONS:

Matthew Jemielita, Michael J Taormina, April DeLaurier, Charles B Kimmel, and Raghuveer Parthasarathy. Comparing phototoxicity during the development of a zebrafish craniofacial bone using confocal and light sheet fluorescence microscopy techniques. *Journal of Biophotonics*, 6(11-12); 920-928, Dec 2012. doi: 10.1002/jbio.201200144.

Michael J. Taormina, Matthew Jemielita, W. Stephens, Adam Burns, Joshua Troll, Raghuveer Parthasarathy, and Karen Guillemin. Investigating bacterial-animal symbioses with light sheet microscopy. *The Biological Bulletin*, 223(1); 7-20, 2012.

H. Linke, BJ Aleman, LD Melling, MJ Taormina, MJ Francis, CC Dow-Hygelund, V Narayanan, RP Taylor, and A Stout. Self-propelled Leidenfrost droplets. *Physical Review Letters*, 96(15); 154502, April 2006. doi: 10.1103/PhysRevLett.96.154502.

ACKNOWLEDGEMENTS

Many thanks are in order to those who have helped along the way. Matt Jemielita, in one way or another, has been involved in many of the technical and experimental work presented in this dissertation and is taking on the subject matter of chapter IV in a thorough and impressive manner. I look forward to seeing him complete the story. A number of colleagues from the biological sciences have helped on many fronts, from collaborating on experiments to general fish husbandry and microbiology. I want to thank John Dowd and Rose Sockol for help with fish husbandry and animal use procedures ; April DeLaurier, Josh Troll, Jennifer Hampton, Adam Burns, and Zac Stephens for experimental collaboration and useful discussion; and Eric Corwin, Andrew Loftus, Tristan Hormel, Ryan Baker, Rick Suhr, and Gary Rondeau for useful disscussions. Special thanks are in order to Karen Guillemin for opening her lab to me and guiding microbial colonization studies. Finally, I would like to especially thank Raghuveer Parthasarathy for allowing me to join his group and carry out interesting and engaging scientific research at the University of Oregon. His experience and advising have been formative for myself as a scientist.

Thank you, one and all.

TABLE OF CONTENTS

Chapter Page

Chapter Page

LIST OF FIGURES

Figure Page

Figure Page

LIST OF TABLES

Table Page

CHAPTER I

INTRODUCTION

By integrating techniques to measure forces, motion, and electrical and chemical potentials with the quantitative application of optical microscopy, the field of biophysics has made significant contributions to the understanding of how physical laws impact living systems [1–5]. The customary focus of the field to push the spatial and temporal resolution of these techniques down to the single molecule or cell brings precision and specificity at the expense of biological context (mostly performed *in vitro*) and scale. This leaves much to be learned by studying biological systems, *in vivo*, on the scale of multicellular organisms in a quantitative, physics guided framework. A shortage of experimental tools that access this intermediate scale therefore brings new challenges for microscopy, instrumentation, and image analysis. To this end, I implement a fluorescence microscopy technique (light sheet microscopy) suitable for examining the space and time scales pertinent to system level phenomena in common model organisms, develop its use in previously inaccessible systems of study, and introduce a method of measuring fluid mechanical properties within such systems via magnetically accessible probes *in vivo*.

Systems in developmental biology, in particular, offer an abundance of complex and emergent phenomena that take place on length and time scales that are much greater than those characteristic of single cells and yet small enough and fast enough to be governed by the collective action of individual members of a large, multicellular population. Studying systems at this intermediate scale necessitates resolution sufficient to distinguish individuals, a field of view large enough to accommodate several thousand of them, the ability to image faster than an individual's motion, but also for long enough to capture the emergent behavior of the group. The fact that life happens

Developmental process	Resolution (μm^3)	Scale (μm^3)	Speed	Duration	Studies
Cell migration	$0.5 \times 0.5 \times 3$	$10^3 \times 10^3 \times 10^3$	$90s$	$10hrs.$	[6, 7]
Cell intercalation	$0.2 \times 0.2 \times 1$	$150 \times 150 \times 50$	$1min.$	$10hrs.$	[8]
Endoderm cell migration	$0.8 \times 0.8 \times 1$	$10^3 \times 10^3 \times 10^3$	$10s$	$2hrs.$	[9]
Heart development	$0.3 \times 0.3 \times 0.65$	$10^2 \times 10^2 \times 10^2$	$10ms$	$12hrs.$	[10–12]
Gut dynamics	$0.2 \times 0.2 \times 1$	$10^3 \times 50 \times 50$	$120s$	$10hrs$	(this work)

TABLE 1.1. Recently studied developmental processes occurring at intermediate spatiotemporal scales. In all cases, high resolution is necessary over large length scales. Time scales are set by how rapid individuals move, as well as the time necessary to witness large scale morphological change. Resolution is listed as lateral (isotropic) by axial.

in three dimensions further demands that imaging it should follow suit, and it is only recently that technology has enabled the tools necessary to study these systems *in vivo*. Table 1.1 lists several examples of recently studied developmental processes where collective and organized behavior of many cells remains poorly understood.

1.1. Model organisms in development

In choosing a model organism with which to study development, one is faced with a handful of options. The roundworm *Caenorhabditis elegans* provides a simple, transparent anatomy with a completely known neural map. *Drosophila melanogaster*, the fruit fly, possesses many genetic tools, as well as an ease of maintenance and husbandry. The zebrafish *Danio rerio*, being a vertebrate, has many processes that are closely conserved in humans, while remaining accessible to genetic and optical tools. Mice are even more closely related to humans (as mammals), while bringing an unparalleled amount of genetic tools to the researcher (accounting for 97% of procedures involving genetically altered animals [13]), at the cost of more complicated maintenance, husbandry, and an internal imaging. In order to help illustrate how closely each model organism is related to humans, I note that we are separated from

mice by approximately 100 million years of evolution, from zebrafish by 400 million years, and insects/nematodes by 600 million years.

In this dissertation, the model organism *Danio rerio* (zebrafish) will be of primary concern as it provides a number of benefits, which will be outlined in the following section. Foremost in reasons for this choice above *C. elegans* and *Drosophila melanogaster* is that the zebrafish, as a vertebrate, possesses many developmental processes which are known to be at least partially conserved [14]. After developing the technical framework necessary for imaging live zebrafish in the embryonic and larval stages, I will briefly investigate the alleviation of the photo-toxic effects of live imaging made possible by the use of light sheet microscopy. Finally, I will develop two avenues of investigation to gain insight into the complex system of a host and its developing microbiome. The first is an image based survey of the growing population of microbes inside the gut of the host, attempting to capture spatial organization and expansion. The second is a technique for directly measuring the material properties of the environment where this colonization takes place.

1.2. The Zebrafish as a Model Vertebrate

The University of Oregon Institutional Animal Care and Use Committee approved all work with vertebrate animals.

It is worth first taking a moment to describe the living system that will be of particular importance throughout this work, motivating its use by listing its virtues, as well as acknowledging its limitations that lead to technical challenges which must be overcome. As mentioned previously, I will use the zebrafish as the model organism of choice throughout the current studies. In the larval stages, the zebrafish (as shown in Figure 1.1) is approximately 2 mm long, 0.5 mm tall, and 0.5 mm thick. Developed as a model vertebrate at the University of Oregon by George Streisinger and colleagues

beginning in the late 1960s, the zebrafish is well suited to developmental studies for several key reasons [14]. First, genetic manipulation of the species has led to the development of numerous mutant and transgenic lines that offer both insight into vertebrate gene function (and disfunction) and incorporation of useful foreign genes, e.g. yielding fluorescent labels of cellular function and lineage. Additionally, in their early stages, larval zebrafish are reasonably transparent, facilitating the use of optical microscopy (both traditional and fluorescent) to study developmental processes noninvasively [15, 16]. Unlike other vertebrate models such as mice, zebrafish are produced in large numbers (typically hundreds of embryos per crossing) and have a more rapid life cycle, allowing the collection of data from a large number of individuals without *a priori* excessive time and maintenance. Finally, an important attribute for the current study is the ability to rear zebrafish germ-free, that is, without any colonizing bacteria present. This is a relatively recent addition to the zebrafish repertoire, being developed in the last decade [17, 18].

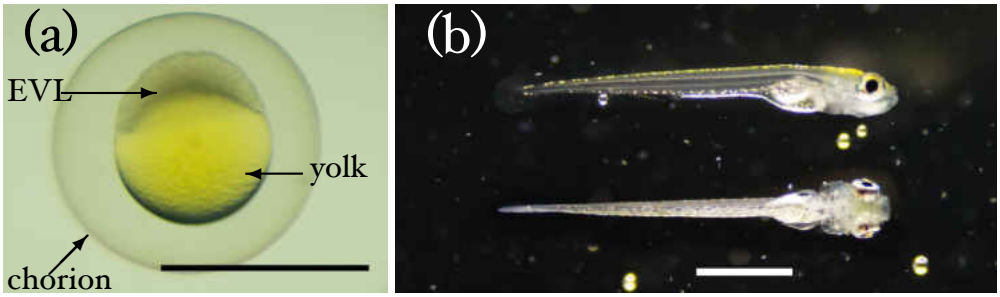

FIGURE 1.1. Microscope images of a zebrafish embryo (a) and larvae (b) at approximately 4.5 hours and 8 days post fertilization, respectively. In (a), the yolk, chorion, and enveloping layer of cells (EVL) that will soon migrate are indicated with arrows. Larvae are shown in lateral (top) and ventral (bottom) orientations. Scale bars are 1mm.

While possessing many key attributes that will facilitate experimental design, it is also worth noting that some properties of the zebrafish present challenges. As

mentioned above, compared to other vertebrate model organisms, the zebrafish is quite transparent in its larval stages. Still, when compared to simpler organisms such as *Caenorhabditis elegans*, it has several disadvantages in optical clarity. First, larval zebrafish are thick enough that objects which are deep within sample can be noticeably distorted by the surrounding tissue. This largely stems from the fact that, as multi-cellular organisms, larval zebrafish are optically inhomogeneous, being composed of many differentiated cell types whose indices of refraction are not generally matched. Additionally, larval zebrafish begin to develop dark patches of pigment, mainly along the dorsal and ventral lines. Depending on the orientation of the fish with respect to the viewer, these spots can obscure either fluorescence excitation light or the transmitted or emitted light that is meant to form an image. In order to minimize the deleterious effects of these spots, one must consider the method of illumination/detection, as well as the orientation and viewpoint of the region of interest within the fish.

Another imperfection with regards to imaging zebrafish are the many sources of unwanted background fluorescence in various tissues and biological materials inside the fish. For example, larval zebrafish live off of a yolk until around eight days post fertilization. This yolk material is particularly auto-fluorescent when excited with wavelengths of light commonly used to excite fluorescent proteins, which are the target of many imaging studies. Another material that produces a strong auto-fluorescent signal is the intestinal mucus of the larval zebrafish gut. This signal is of particular importance for the studies presented in chapters IV and V because it complicates image segmentation in the region of interest in a manner that is not spatially or temporally uniform or predictable. Although these are examples of issues that can complicate optical imaging within the zebrafish model system, none are

insurmountable and a suitable strategy of preparation, experimental design, and post processing can typically be employed to yield useful results. The subject of chapter II will be to outline a specific microscopy technique, known as light sheet microscopy, that addresses some of these challenges, as well as constraints on imaging parameters such as resolution, optical sectioning, speed, and implementation. Chapter III will provide a quantitative comparison of one benefit of this technique to the more common strategy of confocal microscopy in the developing zebrafish system. Next, chapter IV will explore the implementation of light sheet microscopy in a system which would be impractical to image with other methods, namely the bacterial colonization of an initially germ-free zebrafish over a period of tens of hours. Finally, chapter V will develop a method of taking physical measurements of fluid properties within the intestinal bulb of a developing zebrafish.

Portions of Chapters II, III, and IV include co-authored material, which has been previously published.

CHAPTER II

LIGHT SHEET MICROSCOPY FOR LIVE IMAGING IN DEVELOPMENTAL SYSTEMS

In its most basic form, a microscope is the combination of a light source that illuminates an object of interest, a lens that gathers and shapes the light transmitted by the object, and a detector that collects the result and processes it into a representative image (the combination of an eye and brain or a camera and computer, for example). At each step along the way, the expected image can be corrupted, e.g. by the physical behavior of light as it passes through each component of the system or imperfections in the fidelity of the detector. Luckily, these three stages of image formation also each offer the opportunity to intervene and filter the information in a way that is beneficial to the end result. What makes any particular type of microscopy unique and well suited to a specific problem is how the information about the object is treated at each step.

Fluorescence microscopy is one technique that has become ubiquitous because it facilitates many of the more advanced methods described below. In fluorescence microscopy, an object is first illuminated with one particular wavelength of light (*excitation light*). Specialized elements within the sample (natural or engineered proteins or quantum dots, for example) absorb this light and re-emit light at a different wavelength (*emission light*). Filtering out the excitation light and allowing only the emitted light to reach the detector allows an image to be formed based on the locations of fluorescent sources only. Judicious introduction of fluorescence into a sample allows

one to image, for example, specific cell lineages, gene regulation, or foreign tracer particles [19, 20].

Because fluorescence microscopy results in a collection of images of light emitting point sources within the sample (note, however, that these point source images still cannot beat the limit of diffraction and therefore do not yield the actual location of fluorescent reporters with arbitrary precision), additional strategies may be employed to further enhance image formation. Specifically, fluorescence microscopy enables the optical reconstruction of three dimensional images. The challenge of three dimensional microscopy essentially lies in the asymmetry of the resolution in an optical system: a point may be tightly focused in the lateral direction while extending a great distance in the axial direction, contributing to a loss of contrast in adjacent focal planes. In order to recover axial resolution, this effect can be alleviated in one of a few different ways, the most common of which is confocal microscopy, which takes the strategy of filtering information while it is still encoded in the transmitted light, after leaving the object but before detection. This is done by placing a small aperture in the image plane, which is used to select well focused light and reject contributions to the image originating from out of focus regions (as shown in Figure 2.1a). This not only improves the lateral resolution, but the axial resolution as well, allowing the acquisition of images suitable for *optical sectioning*. Because the axial resolution in a confocal setup confines the imaged light in three dimensions, repeating the procedure for many points can build a three dimensional image. Optical sectioning can also be accomplished by instead filtering the illumination light, which is the strategy of light sheet microscopy (illustrated in Figure 2.1b) and the focus of the following sections. There are many more examples of microscopy techniques that are beyond the scope of this text, employing different types of filters at different stages of image formation (structured

illumination [21, 22], super resolution [22], and adaptive optics to name a few) and it should be noted that each has its own set of trade-offs in speed, resolution, and sample preservation. A successful implementation of any microscopy system will involve a well tuned combination of techniques, tailored to the system of study and needs of the research question being addressed. The details of how confocal microscopy and light sheet microscopy differ in their capabilities of live imaging in developmental systems will be further explored in chapter III, for now I will focus on light sheet microscopy and how it is implemented.

2.1. Light Sheet Microscopy

Image-based biophysical studies at multicellular scales don't necessarily require the few-hundred-nanometer or better spatial resolution of sub-cellular investigations, but rather present different challenges. Specifically, the ability to image a large field of view (>100 $\mu m\times$ 100 $\mu m\times$ 100μm) on time scales of seconds to minutes (to avoid cellular motion) for durations of hours to days (to capture large scale development). For example, in order to study full-scale embryogenesis of a zebrafish, one needs to track the movement of approximately 16,000 cells with 0.5 micron lateral resolution and 3 micron axial resolution, through a volume on the order of 1,000 $\mu m\times$ 1,000 $\mu m\times$ 1,000 μm in under 90 seconds, equating to 10 million sampled image points per second. Additionally, this must be accomplished with as little light-induced damage to the specimen as possible, so that it may be repeated for the tens of hours necessary for an embryo to progress through complete developmental stages. Light sheet microscopy is an imaging strategy developed to meet these criteria and has been used with great success to study a wide variety of processes in development, including most of those listed in table 1.1.

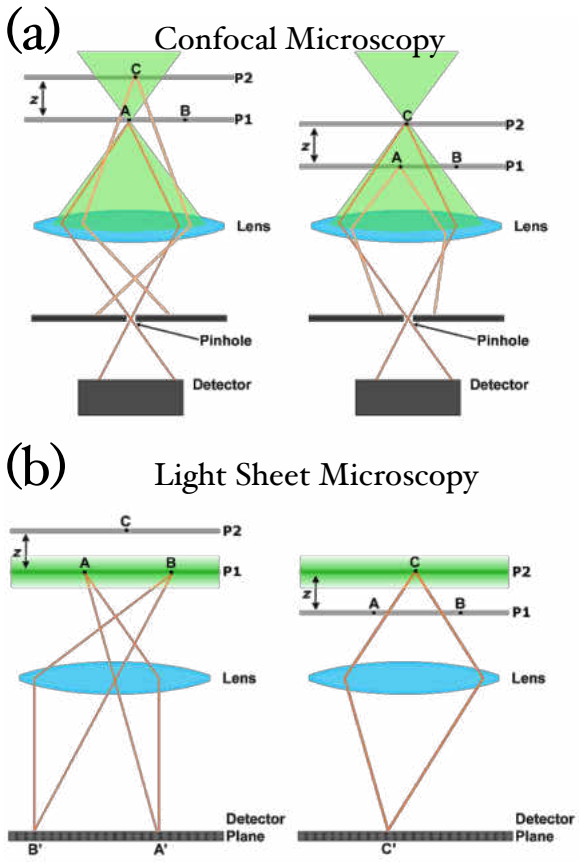

FIGURE 2.1. Schematic illustrations. (a) The geometry of confocal microscopy. As point A in plane P1 is imaged, non-imaged point C in plane P2 is subject to illumination, while its emission is blocked by the confocal pinhole. The converse occurs during the imaging of point C. (b) The geometry of light sheet microscopy. The plane of excitation light is coincident with the focal plane of the imaging objective, allowing a correspondence between illuminated and imaged points.

2.1.1. Strategy

As mentioned above, light sheet microscopy accomplishes optical sectioning by shaping the illumination light (in this case it is fluorescence excitation light) within the sample. Unlike confocal microscopy, which excites fluorescence throughout a large volume and subsequently rejects out of focus emission light (as in Figure 2.1a), light sheet microscopy aims to only excite fluorescence within the focal plane of the imaging system. This is done by creating a thin plane of light (a "sheet") that is co-incident with the focal plane of an imaging objective and camera, which capture a single, two-dimensional image of fluorescence (see Figure 2.1b). Because it acquires all pixels within an optical section simultaneously, its speed advantage over a scanning confocal microscope grows as the number of pixels that make up each slice of a three dimensional image. Also, since no fluorescent marker is excited without being imaged, there is an advantage in total light exposure over confocal imaging that scales as the number of images gathered in the axial direction of imaging.

2.1.2. Implementation

Creating a thin sheet of excitation light can be accomplished in one of a few ways. Our design closely follows others in the literature [7, 23] because of its ease of implementation, flexibility, and that it permits the future integration of advanced techniques such as structured illumination [24, 25], non-Gaussian beams [26], and multi-photon fluorescence excitation [23]. This design, illustrated in Figure 2.2, uses a fast scanning mirror to create a time-averaged sheet of light, which is focused by a low numerical aperture (NA) objective (*excitation objective*) into the focal plane of a second, high NA objective (*detection*, or *imaging objective*). Excitation light can be

rapidly modulated in both power and wavelength by using an acousto-optic tunable filter with an input of several co-linear laser excitation sources.

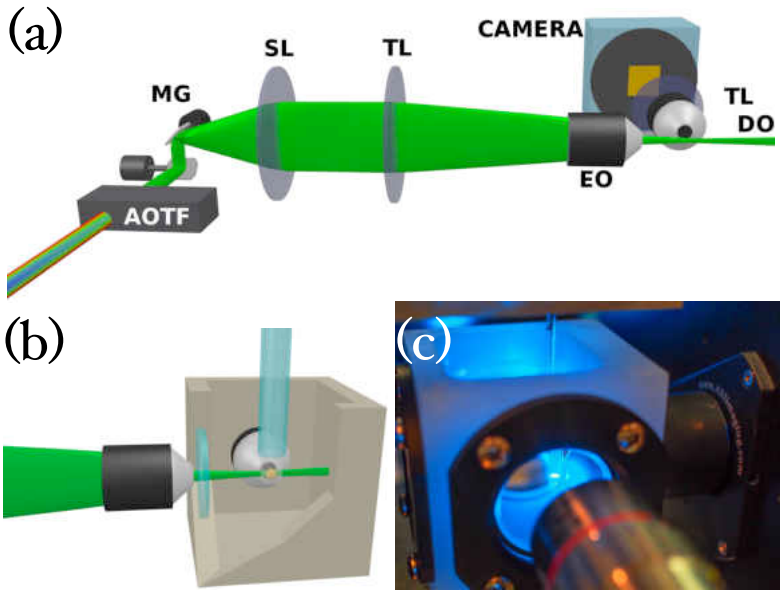

FIGURE 2.2. (a) Schematic of light sheet microscope components showing multiple laser excitation sources, acousto-optic tunable filter (AOTF), mirror galvanometer (MG), scan lens (SL), tube lenses (TL), excitation objective (EO), detection objective (DO), and camera. (b) Schematic of sample chamber (with cut away) illustrating the positioning of a sample (yellow sphere) mounted in agarose gel, which is suspended from above by a glass capillary. The detection objective breaches one wall of the chamber, which is filled with water, while the excitation objective focuses a laser source through a window onto the focal plane. (c) Photograph of the sample chamber with the excitation objective in the foreground, detection objective on the right side of the sample chamber, and glass capillaries entering from above.

The reason to choose a low NA lens for the excitation objective stems from the diffractive nature of light. In order to accomplish the task of optical sectioning, one would like to confine the light to the two-dimensional focal plane as much as possible. However, one cannot arbitrarily focus a light source in this way. For a Gaussian beam the distance that light will propagate before expanding radially by a factor of $\sqrt{2}$ is called the Rayleigh length and is given by $z_r = \pi w_0^2/\lambda$, where w_0 is the beam waist at its narrowest point and λ is the wavelength. Therefore, the tighter the beam is focused,

the faster it will subsequently spread out; one must choose between having a highly confined or a highly uniform excitation profile. Since our goal is the imaging of large scale (as defined above) phenomena, using a low NA objective (Mitutoyo 5×, 0.14NA long working distance objective) to create the light sheet relaxes the confinement of our optical sections in order to obtain larger regions of interest. For excitation light with a wavelength of 488 nm (e.g. for green fluorescent protein), this numerical aperture can produce a minimum sheet width of ≈1.7 μm, setting the limit on axial resolution of optically sectioned images. Under normal operating parameters, our microscope has a sheet thickness of ≈3 μm within the imaging plane. On the detection side, we face no such restriction on NA directly, but what we do need is a long enough working distance (the distance from the front of the objective to its focal plane) to image deep into a sample. For this lens, we can simply choose the highest NA objective that has a working distance of a few millimeters.

We also need to pay attention to how densely we can sample the image, which is affected by both the detection objective and the camera. In order to accurately reproduce a signal, detectors that sample in a periodic manner (such as the array of pixels in an electronic camera) must do so at a rate that satisfies the *Nyquist criterion* (sampling must occur at a rate greater than twice that of the signal itself) [27]. Data that fails to meet this criterion, will posses an artifact known as *aliasing*, where false patterns of longer wavelength emerge in space or time. Common examples of this phenomenon include photographs of brick buildings, striped clothing, and the slow apparent movement of car tires of helicopter blades (the last two examples are of under-sampling in time rather than space). Since the resolution of an optical system has an inherent limitation which is set by the diffraction of light (given by Abbe in 1873 as $d \approx \lambda/2NA$), allowing this distance to cover at least two pixels will ensure that the

Nyquist criterion is satisfied for all resolvable structures. Our camera has pixels that are $6.5 \times 6.5\ \mu m^2$, which is typical for scientific grade CCD and CMOS cameras. We do not want to under-sample an image, which will lead to the deleterious effect of aliasing, but an excessive amount of over-sampling will result in a decreased field of view. Choosing a magnification of $40\times$ (at a high NA) keeps our sampling above the Nyquist rate, while imaging a $416 \times 351 \mu m^2$ field of view. For these reasons, we chose to use a Carl Zeiss $40\times$, 1.0NA water immersion objective (part number 421462-9900-000).

2.1.3. Sample Preparation and Imaging

The optical design of our microscope, having two orthogonal objectives, along with our choice of studying an aquatic organism, makes it convenient to hold the sample from above, submerging it into a temperature controlled, water filled sample chamber. A zebrafish is first anaesthetized (as in [28]) and placed into a 0.05% solution of liquid agarose. The fish is then drawn into a small glass capillary such that it is oriented vertically and the agarose is allowed to cool through its gel transition. Now the capillary can be held on a three-axis stage (Applied Scientific Instrumentation, Eugene, OR), and a small amount of gel containing the fish is extruded out the end of the capillary and into the excitation light (see figures 2.2b/c and 2.3a). In order to produce a three-dimensional image, the sample is translated through the light sheet as images of individual planes are collected.

This arrangement, as illustrated in Figure 2.2b/c, imposes design constraints on the sample chamber itself. First, the imaging objective should be the water immersion type which can have its front element submerged in the water-filled chamber from the side. This necessitates creating a water-tight seal around the barrel of this objective, which can be done in a number of ways. What one has to keep in mind is that the design of

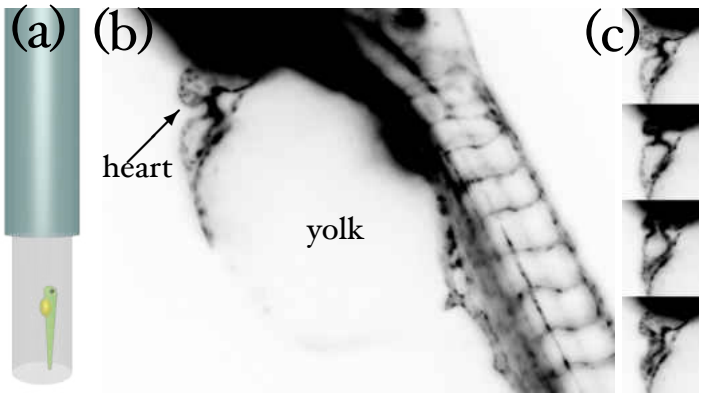

FIGURE 2.3. (a) Illustration of zebrafish mounted in agarose gel, extruded from the end of a borosilicate glass capillary. The capillary is attached to a three-axis stage, capable of translating the fish through the light sheet in order to acquire images at different planes within the sample. (b) Example optical section of a zebrafish image in the fluorescence light sheet microscope (intensity inverted), indicating the yolk and heart. (c) Time series of heartbeat from panel (b), viewed in one optical section.

the microscope may necessitate motion of one or both objectives for the purpose of focusing, alignment, or scanning. If motion is necessary, conventional sealing methods, such as with an o-ring, are unlikely to be the optimal. One can instead employ a flexible sheet of material such as silicone rubber clamped to the sample chamber and somehow sealed around the objective (as in [26]). In early iterations, we used a cast-moldable silicone rubber (Mold Max 10T, Reynolds Advanced Material of Hollywood, CA) to make a sheet of rubber with an hole sized to match the barrel diameter of the imaging objective. This could be used as one wall of the sample chamber, clamped to the three adjacent walls to create a water-tight seal. We found this approach to be cumbersome and unnecessary, and have since moved to a design where o-rings provide all of the necessary seals to the chamber for windows as well as imaging optics (the current iteration of sample chamber is shown in Figure 2.2c). Our imaging objective is therefore fixed in relation to the sample chamber. Since the sample is held from above and *not*

fixed to the chamber, the focus can still be adjusted by moving the imaging objective, the sample chamber moving along with it.

Another design parameter is the working distance of the excitation objective, which must be long enough to focus in the middle of the field of view of the imaging objective, while leaving enough room to accommodate the glass windows of the chamber, as well as allow the movement of multiple samples within the chamber. Even by using a low NA objective for this purpose, there are still few commercially available objectives that have a working distance of more than a few centimeters and one must consider the implications of objective choice on sample chamber design.

2.2. Characterization

As mentioned at the beginning of this chapter, any successful microscopy system will balance the trade offs between speed, resolution, and sample preservation. The light sheet microscope that has been constructed for the studies of the following chapters has been designed specifically to study developmental processes and has many capabilities well suited to this avenue of research. We routinely collect three-dimensional images covering a field of $300\mu m \times 1{,}200\mu m \times 150\mu m$, in two color channels, within 120s, for durations up to 24 hours. A lateral resolution sufficient to identify single bacteria is maintained and an axial resolution sufficient to optically section layers of host cells is achieved. Our sample chamber accommodates the imaging of up to six zebrafish larvae in series, allowing one imaging session to gather data on multiple replicates for the purpose of increasing statistics or several different specimen types to screen for variation. This allowance of multiple specimens is a departure from the common practice among research groups performing light sheet imaging, which typically image a single specimen. The trade off here is the inability to perform more

complex imaging strategies to further improve resolution, such as sample rotation and multi-view data acquisition [9, 29]. We believe, however, that in our studies, amassing data from a greater number of zebrafish is more important and that sample rotation is still possible to integrate with multiple samples if needed in the future. Amassing greater amounts of data, however, can pose it's own technical limitations. For example, at the resolution stated above, each three dimensional image contains roughly 2 billion volumetric pixels (voxels) when imaged at 40×. Since each camera pixel has a bit depth of 16, this requires 4 gigabytes (GB) of storage per scan, and 1.7 terabytes (TB) to image the complete gut of six larval zebrafish every twenty minutes for 24 hours. In the best case scenario, the data extracted from these images is straight-forward and can be performed fast enough to do in real time (without writing raw image data to hard disk), as in [9]. Otherwise, raw image data must be stored for subsequent processing, which we do on a large RAID (redundant array of independent disks) file server, with a 60TB capacity. Future microscopy systems for the types of studies discussed here will successfully integrate fast and efficient data processing, made possible through either specialized hardware (such as graphics processing units), advanced image processing techniques, efficient compression algorithms, or a combination of all three.

While improvements can always be made, our current implementation possesses many features that make it suitable for large scale, three dimensional imaging of systems such as those to be described in the remaining chapters. Despite the large field of view, we maintain the ability to visualize single bacteria cells and morphological properties of individual host cells 2.4. The imaging speed is fast enough to image the entire gut of a larval zebrafish in between peristaltic waves, but can lag behind the rapid swimming of individual bacteria within it (in three-dimensions). This is not to say that the method is slow, on the contrary, it is much faster and gathers light more efficiently than a confocal

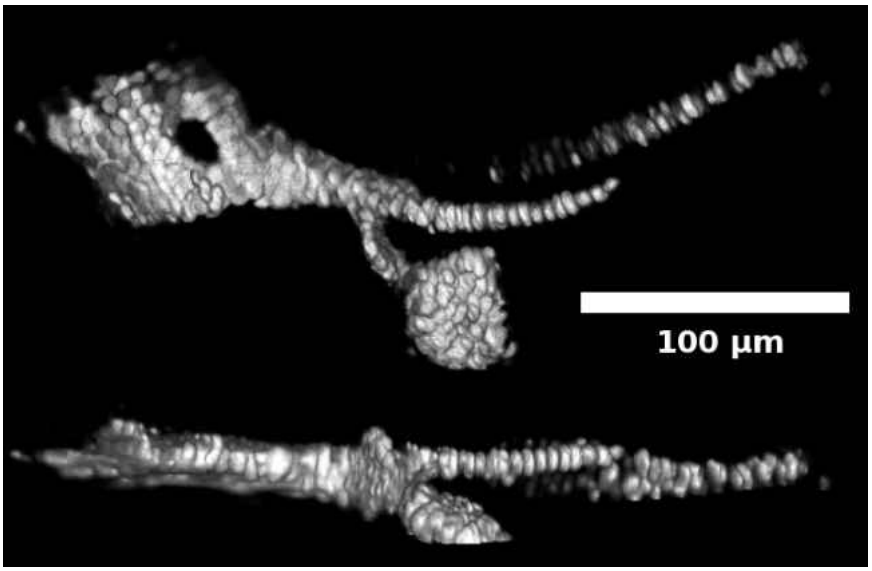

FIGURE 2.4. Representative three dimensional image obtained in the light sheet microscope showing fluorescently labeled cartilage cells forming the hyosymplectic in a 72 hpf zebrafish larva from the lateral (top) and ventral (bottom) vantages. Individual cells are roughly 10 microns in size.

microscope, the implications of which affect not only the acquisition of single time point images, but also the damage incurred by the specimen when imaged over long periods of time. In the following chapter, I will further investigate this idea of *phototoxicity* and how it can manifest differently under these two types of imaging strategies.

CHAPTER III

PHOTO-TOXIC EFFECTS OF LIVE IMAGING IN CONFOCAL AND LIGHT SHEET FLUORESCENCE MICROSCOPY

As noted in chapter II, three dimensional fluorescent imaging of embryonic development can be accomplished in different ways. The most common approach has been that of confocal microscopy, which has matured into a robust and powerful method, with commercially available implementations and application specific enhancements. While effective, confocal microscopy in all its forms is intrinsically inefficient in its use of light. Large volumes outside the focus are illuminated, and hence subject to photodamage, without providing information on specimen structure (Figure 2.1). By contrast, light sheet microscopy (equivalently known as selective plane illumination microscopy (SPIM) [30], digital scanned light sheet microscopy (DSLM) [7], and other names [31]) involves the illumination of a specimen within a thin volume, confined to the focal plane of a widefield detection scheme that collects the resulting fluorescence emission. The sectioned plane is imaged at once, without scanning, onto a camera, and a three-dimensional image is formed by translating the specimen relative to the sheet in the dimension perpendicular to the plane (figures 2.1 and 2.2) [7, 26, 31–33]. The light sheet geometry enables a one-to-one correspondence between points in the specimen that are illuminated and points that are imaged (Figure 2.1)). While it has been previously shown that this efficient use of light leads to orders-of-magnitude less photobleaching than confocal or multi-photon microscopies [7], it is not well established whether SPIM significantly minimizes

morphological abnormalities in developing animals. In other cell-biological contexts it is increasingly realized that photodamage can significantly alter cellular function even in the absence of obvious readouts such as photobleaching [34]. We suggest that this lesson applies to developmental processes in animals as well, and that light sheet microscopy provides a much-needed route to less-perturbative imaging of embryos.

The anecdotal evidence of colleagues suggested that capturing the morphogenesis of bone on a cellular level without phototoxic side effects could be challenging. Furthermore, the mechanisms by which bones develop into stereotypical shapes remain poorly understood, due in large part to the difficulty of imaging bone growth over developmentally relevant times with sufficient temporal resolution to visualize cellular processes and with identification of particular cell types [35]. In order to test the idea that light sheet fluorescence can alleviate some of these effects, we therefore chose to examine the issue of phototoxicity affecting development by studying skeletal morphogenesis in zebrafish larvae.

As a specific skeletal target for studying bone development, we investigated in zebrafish the early development of cells generating the opercle, a craniofacial bone that forms part of the gill covering and that undergoes considerable shape changes during the first few days post fertilization [36–38]. The opercle begins to develop around 2.5 dpf, initially as an elongating "spur" (Figure 3.1a). Between 72 and 96 hours post-fertilization, the opercle widens at its posterior end, forming a fan-like shape, as illustrated in Figure 3.1a. To track opercle development and the behavior of osteoblasts, the cells that make bone, we studied a transgenic zebrafish line containing an insertion of the enhanced green fluorescent protein (EGFP) gene downstream of the regulatory regions of the osteoblast-specific zinc finger transcription factor *sp7* [35]. The time interval between three-dimensional snapshots of opercle-forming osteoblasts

determines the developmental processes that can be probed. Twenty minute intervals, for example, can provide information about modes of large-scale shape formation such as elongation and widening, but finer temporal sampling is necessary to resolve cellular behaviors such as recruitment, migration, and rearrangement. We found normal

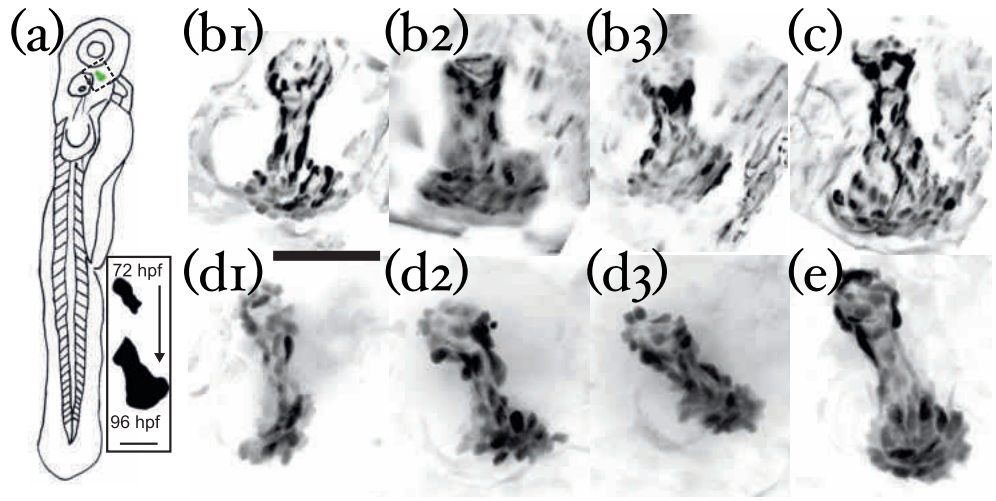

FIGURE 3.1. (a) Schematic of a 3 dpf zebrafish; the dashed box outlines the developing opercle. Inset: the characteristic opercle shape at 72 and 96 hpf. Scale bar: $50\mu m$. (b-e) Maximum intensity projections of 3D fluorescence images of EGFP-expressing osteoblast cells at 96 hpf. Image intensities have been inverted for clarity. The posterior end of each opercle points toward the bottom of teh panel. b1-3 and d1-3 show three different specimens each imaged once every ten minutes for the preceeding 24 hrs. with light sheet and confocal microscopies, respectively. Panels c and e show control specimens for light sheet (c) and confocal (e) data sets, imaged only at 96 hpf. Scale bar: $50\mu m$.

opercle development for specimens subjected to spinning disk confocal imaging over 24 hours beginning at 72 hpf with twenty minute intervals between three-dimensional images, but highly abnormal shapes when ten minute intervals were used, indicating significant phototoxicity. In contrast, light sheet imaging with ten minute intervals and the same light exposure per imaged point as the spinning disk experiments consistently yielded opercle morphology identical to that of non-imaged controls. Quantifying opercle shape at each time point, we found that opercles subject to short-interval

confocal imaging grow continuously in length but fail to initiate widening perpendicular to their long axis, an important developmental step which is evident in light sheet-imaged specimens. These data, as well as the results of imaging opercles using still shorter intervals, are presented below. We also discuss the imaging of the symplectic cartilage, a different craniofacial structure that shows less sensitivity to photodamage. Our findings suggest that light sheet microscopy offers the potential for studying slow growing organs such as bones with the high temporal density necessary to examine cell-level processes.

3.1. Experimental

3.1.1. Transgenic Zebrafish

The creation and characterization of the *Tg(sp7:EGFP)b1212* transgenic line, which allows the detection of EGFP-labeled osteoblasts in developing zebrafish, is described in detail in [35]. The sox9a^{zc81Tg} transgenic line, which expresses EGFP in cartilage cells, in noted in [39]. Larvae were anesthetized with 80 μg/mL clove oil in embryo medium and mounted for imaging in 0.5% agarose gel.

3.1.2. Confocal Microscopy

Confocal images were obtained on a commercial spinning-disk confocal microscope (Leica SD6000 with a Yokogawa CSU-X1 spinning disk). We examined specimens over a depth of 50 microns with a 1 micron spacing between optical sections, capturing images with an EMCCD camera (Hamamatsu imgeEM) with 100ms exposure time.

The total time required per three-dimensional image using spinning disk confocal microscopy is approximately 20 seconds, which includes both the image acquisition time and the time needed to move between speciemens.

3.1.3. Light Sheet Microscopy

Light sheet imaging was performed on the custom built apparatus described in chapter II and illustrated in Figure 2.2. Images were captured using a scientific CMOS camera (Cooke pco.edge), using custom software written by us in MATLAB. The excitation light was provided by an Argon/Krypton ion laser (Melles Griot 35 LTL 835) with a maximum power of 10mW at 488nm. Light sheet microscopy images were deconvolved using commercially available software (Huygens, Scientific Volume Imaging); the utility of exploiting high contrast and dynamic range of light sheet imaging using deconvolution has been noted previously in [40].

The total time required per three-dimensional image using light sheet microscopy is approximately 14 seconds, which includes both the few-second image acquisition time and the time needed to move between specimens. In all experiments, we imaged in sequence six larval zebrafish in order to obtain the necessary throughput for adequate statistics, and also to account for the non-negligible chance of mortality exhibited by larval zebrafish. The minimum possible interval between imaging times is therefore $6 \times 14 = 84$ seconds, or 1.4 minutes. Imaging at this instrument-limited rapid rate requires not saving complete image data, in order to avoid the additional constraints of hard-drive writing time. For the 1.4 minute interval data presented here, only maximum intensity projections were saved during imaging.

3.1.4. Equivalence of Exposure Energies

In order to make a valid comparison between the two imaging systems, it is necessary to find some parameter that can be made equivalent between the two. Some choices for this could be to match exposure times, signal to noise in the acquired data, or laser power. These area all affected, however, by the limitations and efficiencies of

hardware and are therefore poor choices to make a comparison between the microscopy techniques rather than the microscopes themselves. For example, signal to noise can be improved by using an electron multiplying charge coupled device camera (EMCCD), which the confocal microscope possesses and the light sheet microscope does not. Since the goal is to test and compare the phototoxicity in the sample, regardless of things like image quality or contrast, we chose to design our experiments such that the amount of optical energy received by any point as it is imaged is equal for the two setups.

For the confocal microscope, we measured the total excitation laser power to be 1.0mW at the location of the objective lens. At 40× magnification, the field of view spans an area of A = $3.0 \times 10^{-8} m^2$ in the focal plane. The spinning disk unit, consisting of rotating disks of pinholes and microlenses [41], has an overall transmission factor T $\approx$ 60% [42]. The power density is therefore PT/A $\approx 3 \times 10^4$ W/m^2, where PT = 1.0 mW is the measured transmitted power. Integrated over the 100 ms camera exposure time, the received energy density at each imaged point during the capture of a single two-dimensional optical section is ϵ = 3 kJ/m^2. As illustrated in Figure 2.1a, each point within the three-dimensional volume also receives excitation light during the exposure of adjacent image planes. For example, during the imaging of point A in Figure 2.1a, the intensity at point C is lower by a factor proportional to z^2, z being the distance between planes P1 and P2. This reduction is countered, however, by the fact that point C also receives excitation light during the imaging of point B, as well as all other points in P1 within an area equal to that previously mentioned. Because of this, every point in the scanned volume receives as much energy during every two-dimensional image acquisition as it does during the imaging of its own plane. The total energy delivered to each point in the imaged volume is therefore higher by a factor equal to the total

number of optical sections obtained during the scan. For the imaging performed during this study, this equates to approximately 150 kJ/m^2 per point in the total imaged volume, 50 times larger than the 3 kJ/m^2 exposure energy experienced by each point while it provides image information.

We operated the light sheet microscope with the total power measured at the illumination objective to be 0.4 mW. The focused laser beam had a thickness of approximately 10μm in the field of view. Rapid scanning of the laser produced a 400 μm wide sheet, corresponding to a power density of 1×10^5 W/m^2. When integrated over a 30 ms camera exposure time, tis gives each imaged point an energy density ϵ = 3 kJ/m^2, approximately equal to that of the spinning disk confocal experiments as described above. As illustrated in Figure 2.1b, any additional exposure during the imaging of other optical sections is intrinsically lower than that of confocal imaging. Moreover, even though the excitation of adjacent planes due to the finite sheet thickness is nonzero, the fluorescence emission it generates will be detected, not blocked, and hence can contribute to image formation via deconvolution.

3.1.5. Morphological Analysis

In order to analyze the changing morphology of the opercle, we segmented [43] three-dimensional image stacks using custom software written by us in MATLAB, determining the pixels corresponding to the osteoblasts and to background. Since the fluorescence intensity of opercle-forming osteoblasts was considerably brighter than the background, we segmented the opercle using a user-adjusted global threshold and then manually removed the few falsely segemented regions. A small number of data sets during which the specimen twitched were omitted from the analysis.

In order to characterize the key morphological feature of normal opercle growth, namely the fanning out of the opercle at its end, we measured the perimeter of cross-sections of the opercle perpendicular to its length. From the segmented volume, we computed the first principle axis of the opercle, i.e. the vector for which the root mean squared distance from points in the segmented volume to points on the vector is minimized, which robustly identifies the long axis of the opercle (Figure 3.2a). At any point along the long axis, we find the set of points in the segmented volume that lie in the perpendicular plane. We define the perimeter as the arc length of the convex hull of this set of points, and evaluate this perimeter at micron-spaced positions along the long axis. In order to reduce the effects of small cellular protrusions on the perimeter measurement we averaged our measurement with a sliding 20 micron window along the long axis. As a dimensionless measure of the "fanning" of the opercle we consider the ratio of the widest to the narrowest perimeter (Figure 3.2b), discussed further in section 3.2. In addition, we record the length of the opercle, identified as the distance between the points at which the principle axis intersects the beginning and end of the segmented volume of the opercle. Using the procedure outlined above we are able to measure gross three-dimensional morphological features of the developing opercle efficiently and without potential biased manual assessment.

3.2. Results and Discussion

We found that opercle growth progressed normally in size and shape, with the fan-like expansion at the ventral end described above and illustrated in Figure 3.1a [36, 37], when specimens were subjected to light sheet imaging over the 24 hours from 72 to 96 hpf with 10 minute intervals separating the acquisition of three-dimensional images. In contrast, opercles imaged using a spinning disk confocal microscope with the same energy density per imaged point (see section 3.1) consistently showed opercle growth

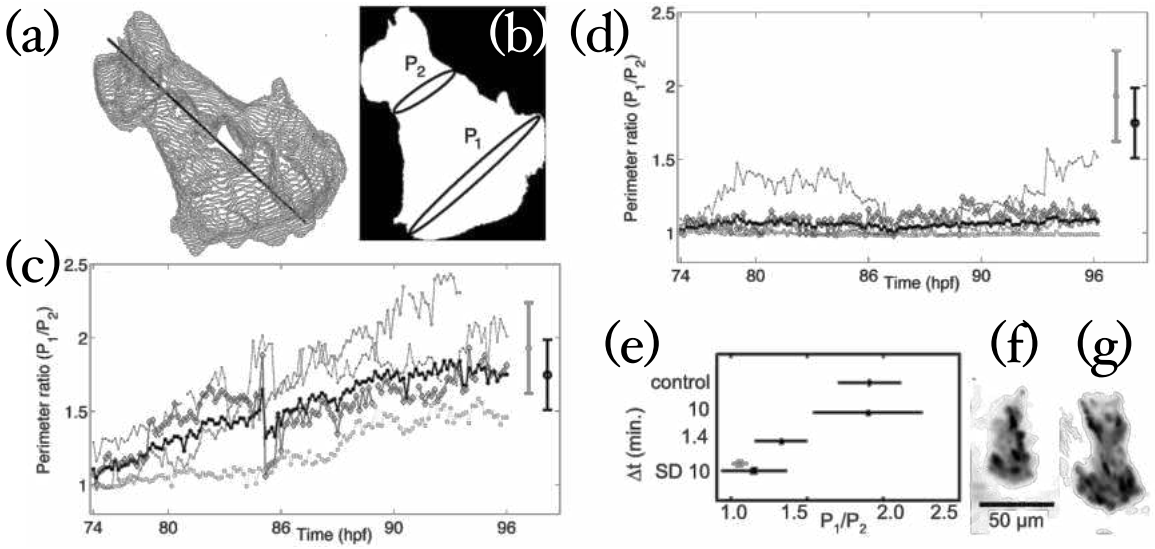

FIGURE 3.2. (a) Surface mesh of a representative opercle, identified by computational image segmentation. The black line is the principle axis of the segmented volume. (b) Schematic showing possible widest, P1, and narrowest, P2, perimeters of the segmented opercle. (c) Perimeter ratio for 74-96 hpf for opercles imaged on the light sheet microscope with 10 minute intervals between data sets (N = 4). (d) Perimeter ratio for 74-96 opercles imaged on the spinning disk confocal microscope with 10 minute intervals between data sets (N = 5). The grey and black data points at the right of panels c and d show the mean and standard deviation for opercles of control fish imaged only at 96 hpf that were (black, N = 10) and were not (grey, N = 12) anesthetized between 74-96 hpf. (e) Comparison of the final (96 hpf) perimeter ratio for different imaging intervals (Δt). Values are plotted for light sheet microscopy data obtained with Δt = 10 minutes (as in (c)). and 1.4 minutes (N = 6). Data from spinning disk confocal microscopy (SD) with Δt = 10 minutes are from the specimens plotted in (d), with all five data points indicated in black, and the set excluding the morphologically aberrant outlier discussed in the text in grey. Control data are from anesthetized, non-imaged specimens as shown in (c, d). (f, g) Maximum intensity projections for two opercles imaged with light sheet microscopy using 1.4 minute intervals, showing the range of fan-like morphology observed.

lacking a fan-like expansion. In Figure 3.1b,d we show maximum intensity projections of opercle-forming *sp7*-expressing osteoblast cells at 96 hpf for representative fish imaged using the light sheet (Figure 3.1 b1-3) and the confocal microscope (Figure 3.1 d1-3). Two representative control fish that were not anesthetized and that were only imaged at 96 hpf are shown in Figure 3.1c and e.

Images from the course of the experimental time lapse illuminate differences in morphology. In Figure 3.3 we show a maximum intensity projection of opercle-forming osteoblasts at different time points for fish imaged with the light sheet (Figure 3.3a) and the spinning disk confocal (Figure 3.3b) microscopes. At 72 hpf both opercles are rod-like in shape. Over the next 24 hours the tip of the opercle imaged on the light sheet microscope begins to fan out as well as lengthen. In contrast, the opercle imaged on the spinning disk confocal microscope lengthens but does not fan out; rather, it remains relatively rod-like in shape over the entire time-lapse. Movie of the 24-hour data sets are provided in [44] as supporting information.

The fish examined in this study were not raised beyond 3 dpf. Our prior experience with opercle imaging suggests that fanning morphogenesis does not resume or recover later in development; there is no sign of normal shape into the second week of development if the opercle undergoes photodamage at 2-3 dpf.

In order to quantify differences in fanning behavior between experimental conditions, we segmented the entire time series for all imaged fish to identify the voxels corresponding to the opercle (see section 3.1). In the stereotyped normal growth of the opercle an initially rod-like collection of cells transforms into a fan-like shape. As a result, for normally growing opercles the ratio of the widest part of the opercle to the narrowest part should increase over time. Using our images, we determined

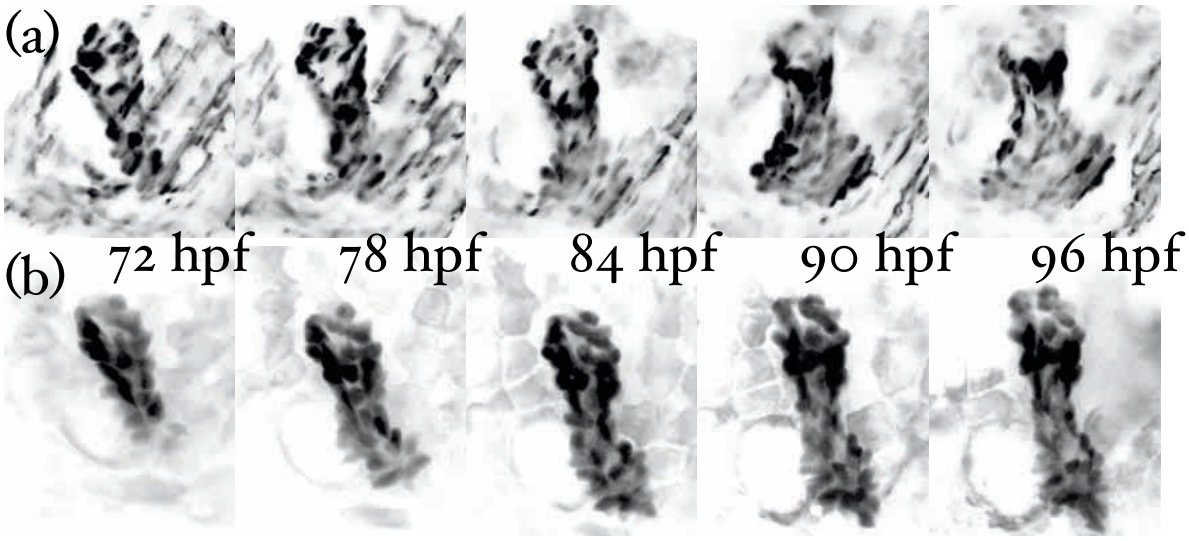

FIGURE 3.3. Maximum intensity projections of three dimensional scans of EGFP-expressing osteoblast cells in a developing opercle, as imaged with light sheet (a) and confocal (b) microscopy using equivalent exposure conditions. Image intensities have been inverted for clarity. One three-dimensional data set was acquired every ten minutes over the course of twenty-four hours; the images shown are separated by six hour intervals. The scale bar is 50 microns in length.

the perimeter of the cross-sections perpendicular to the long axis of the opercle, and calculated the ratio of the largest to the smallest perimeter (P_1/P_2) (Figure 3.2a and b).

In Figure 3.2c and d we plot this perimeter ratio (P_1/P_2) for fish imaged using the light sheet and confocal microscope, respectively. In both panels, the thick black line shows the average perimeter ratio over all samples, while the lighter gray lines are the perimeter ratios for each individual opercle. Over the course of the time lapse the perimeter ratio of fish imaged on the light sheet microscope increases and at 96 hpf is similar to that of the control (non-imaged) fish. In contrast, the perimeter ratio for opercles imaged with confocal microscopy remains, for the most part, close to one, consistent with a shape that remains rod-like over time. There was, however, one fish imaged on the confocal microscope that had an increasing width ratio over the course

of the time-lapse. This fish, shown in Figure 3.1d panel 1, had a different development defect in which the opercle was no longer symmetric.

While the difference in perimeter ratio between the two imaging setups is stark, other morphological features of the opercle remained normal. In Figure 3.4 we show the average length of opercles over the entire imaging period. The length increases similarly for fish imaged using the spinning disk confocal and the light sheet microscope. The greater scatter of data points in the light sheet-derived lengths is likely due to the fan-like lateral expansion of the opercle, which complicates the computational identification of the long (principle) shape axis.

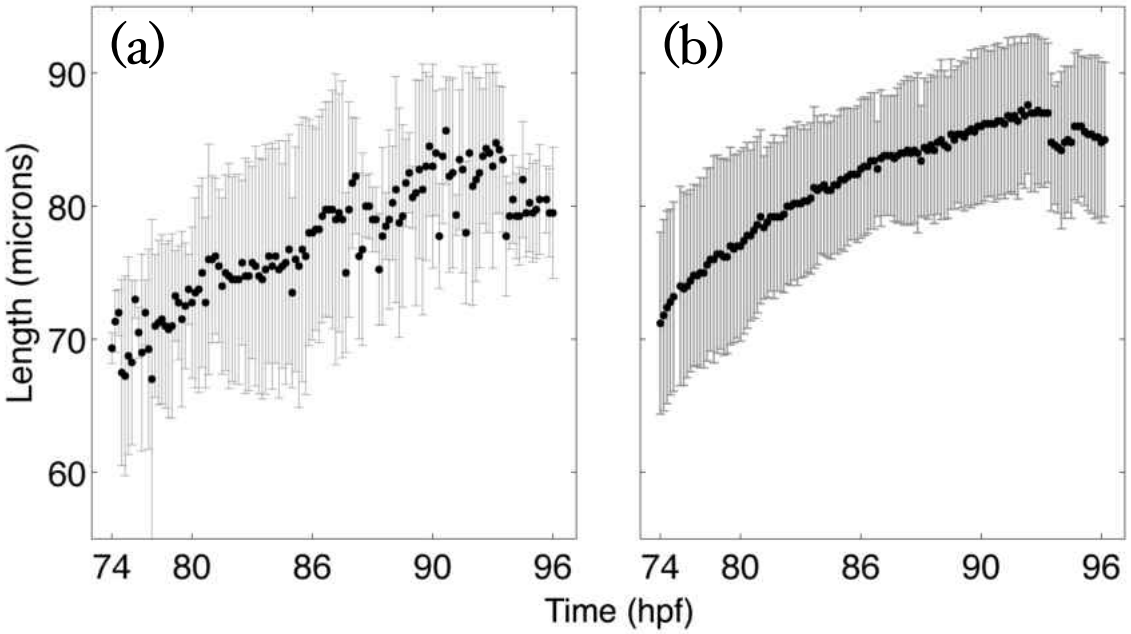

FIGURE 3.4. Mean and standard deviation of opercle lengths imaged on the (A) light sheet microscope and (B) spinning disk confocal microscope from 74-96 hpf.

The similar lengthening and dissimilar widening of opercles imaged with spinning disk confocal and light sheet microscopies imply that the photodamaged opercles follow different trajectories in the space of possible forms than do normal opercles.

This is illustrated in Figure 3.5, in which the perimeter ratio and length data of figures 3.2 and 3.4 are plotted versus each other.

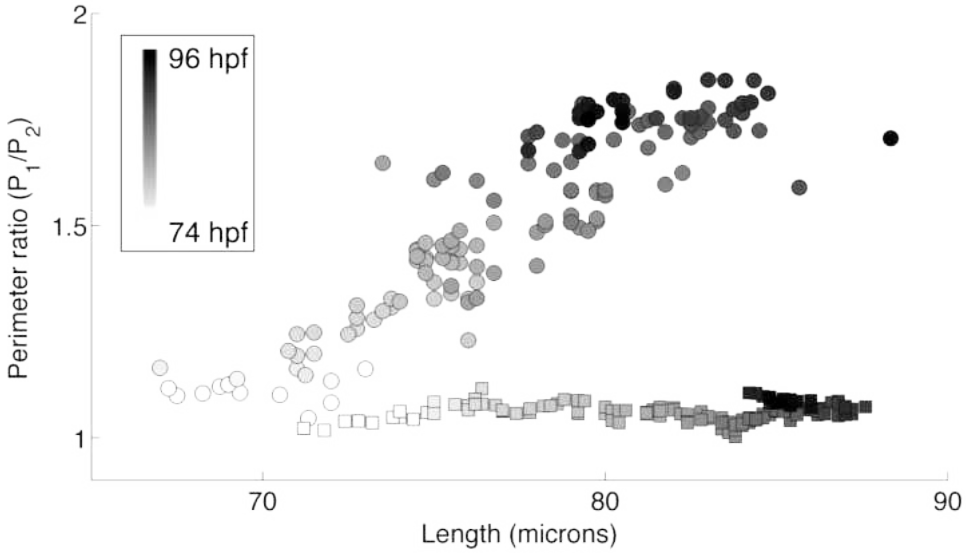

FIGURE 3.5. Mean perimeter ratio vs. mean length for opercles imaged on the light sheet microscope (circles) and the spinning disk confocal microscope (squares). The gray level of the data point indicates the time.

Figure 3.6 shows the average fluorescence intensity for all imaged fish over the course of the time-lapse for the two microscope set-ups, normalized by its value for the first three hours of the experiment. We calculate the intensity as the total pixel intensity in the segmented opercle divided by the volume of the opercle. We find moderate photobleaching for fish imaged using confocal microscopy, with a dimming of about 20% over 24 hours, and no appreciable bleaching for specimens imaged using light sheet microscopy.

While at short (10 minute) time intevals opercle growth is clearly abnormal when imaged using the confocal microscope, if the scan interval is increased by a factor of 2, to 20 minutes, the perimeter ratio increases as expected and the opercles appear morphologically normal (Figure 3.7 and [44]). Since one can capture stereotyped

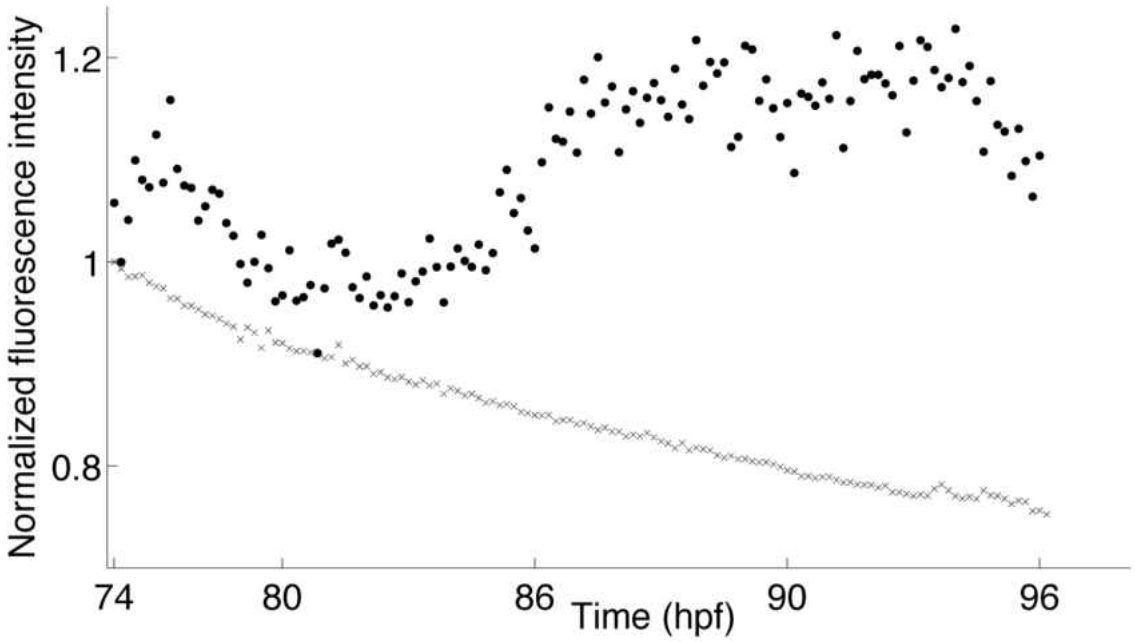

FIGURE 3.6. Normalized fluorescence intensity for fish imaged on the spinning disk confocal (grey crosses) and light sheet (black circles) microscopes. One of the light sheet imaged fish showed a considerable increase in brightness at around 86 hpf, causing the step evident in the plotted specimen-averaged data.

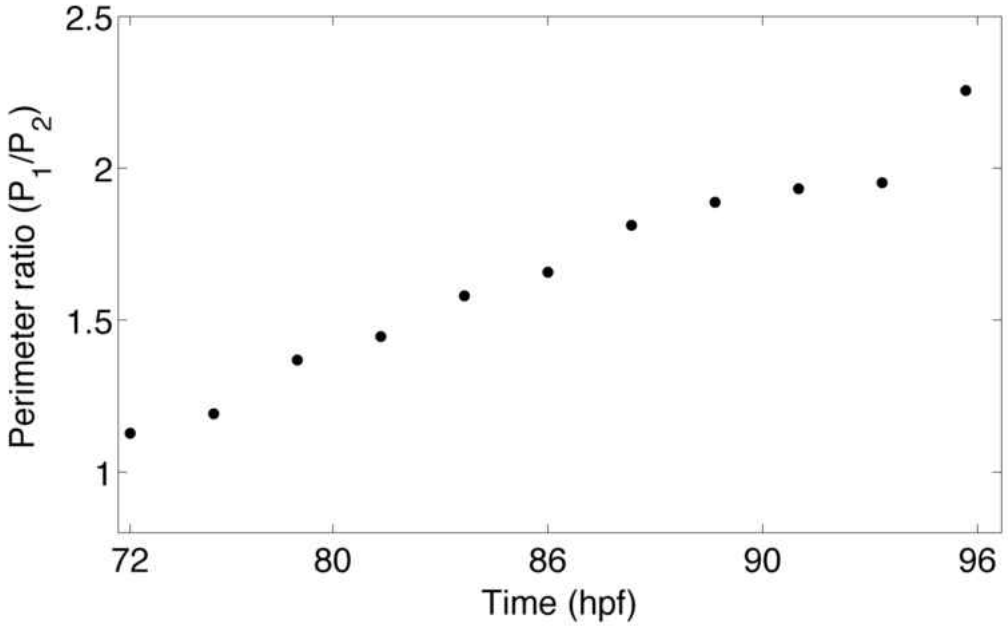

FIGURE 3.7. Perimeter ratio for opercles imaged at 20 minute time intervals using the spinning disk confocal microscope (average, N=4).

opercle growth with this larger time interval, and successfully perform a wide range of studies of skeletal development, one may reasonably ask if there are features of bone growth that can only be captured if the imaging is done at the shorter time intervals, such as the 10 minute intervals used for the data presented above. In Figure 3.8 we show cellular extensions in an *sp7*-expressing osteoblast at the opercle edge, demonstrating projections that change dramatically in size and shape within 10 minutes. Several such protrusions were observed. While we do not speculate on the importance of these protrusions in the development of the opercle, we note that cellular motions and interactions of cells with their neighbors are generally important for multicellular organization. The higher frame rate and lower photodamage of light sheet microscopy makes it possible to capture potentially salient biological processes at very short time scales for extended periods of time.

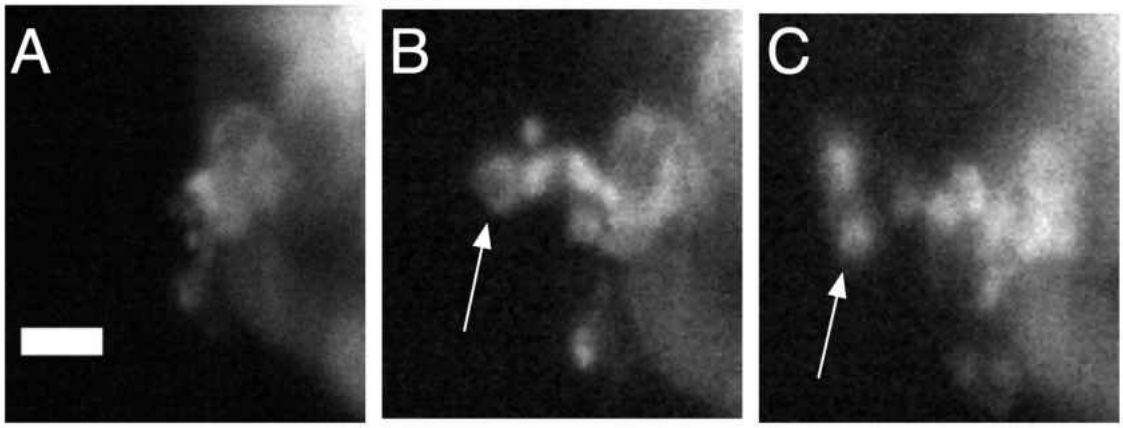

FIGURE 3.8. Extensions of osteoblast cells, indicated by arrows. The time step between panels is 10 minutes. Scale bar: 5 μm.

Conversely, while 10 minute intervals give normal opercle growth under light sheet microscopy, we can ask if this would still be the case with less time between three-dimensional images. With 1.4 minute interval, all specimens examined show fan-like posterior widening of the opercle that is smaller in magnitude than that seen in control specimens, but that is greater than that of 10 minute interval confocal-imaged specimens (Figure 3.2e). While in principle shorter intervals are possible to examine, technical limitation prohibit our exploration of them .

It is important to note that phototoxicity in general may be highly tissue and cell-type specific. We illustrate this by examining the symplectic cartilage, another craniofacial structure that begins to form at a similar time as the opercle, elongating via intercalation of chondrocytes between 55 and 72 hpf [45]. The transgenic sox9a^{zc81Tg} expresses EGFP in cartilage cells [39], allowing visualization of symplectic formation using the same fluorescent protein as employed in the above sp7:EGFP osteoblast imaging. In contrast to the developing opercle, we do not find obvious signatures of photodamage in the developing symplectic, under the same exposure conditions. In

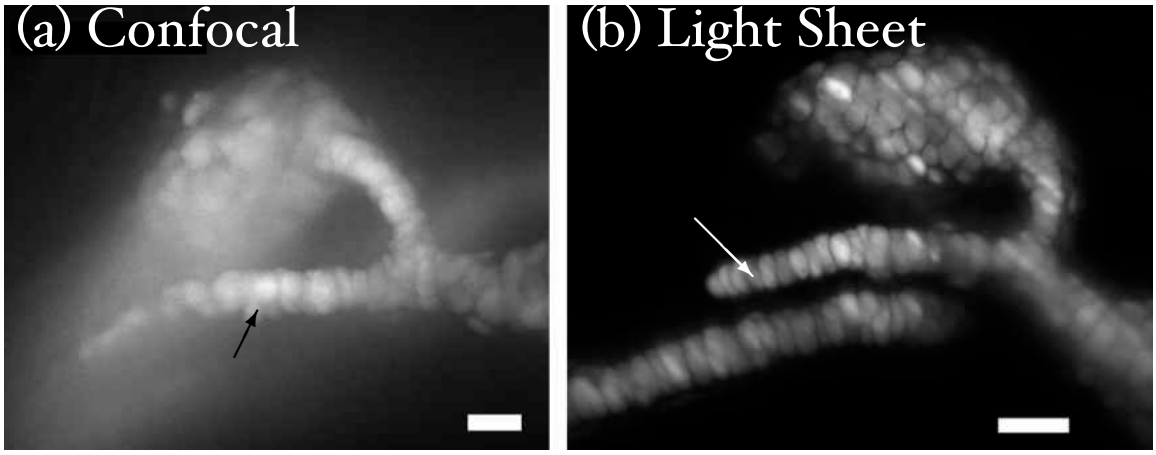

FIGURE 3.9. Maximum intensity projections of 3D scans of sox9a^{zc81Tg}:EGFP showing cartilage including the symplectic cartilage (arrows), using spinning disk confocal (a) and light sheet (b) microscopy with equivalent exposure conditions. One three-dimensional data set was acquired every ten minutes over the course of twenty-four hours; the images shown are from the final time point, at 72 hpf. The scale bar is 20 μm.

spinning disk confocal as well as light sheet studies in which three-dimensional images are obtained at 10 minute intervals for 24 hours with the same setups as described above, we see normal growth of a column of cells (Figure 3.9 and [44]). Interestingly, the normal symplectic growth during this period involves a steady one-dimensional extension. In photodamaged opercles, we found that lengthening along the long axis is not affected by photodamage, but the activation of growth perpendicular to the long axis is inhibited in photodamaged specimens. One may speculate that the lack of obvious photodamage in symplectic growth is related to an absence of particular developmental programs that must be activated during the time span of interest, though we stress that the molecular mechanisms driving these differences are unknown.

3.3. Conclusion

In the past few years light sheet microscopy has emerged as a promising technique for three-dimensional fluorescence imaging due to its high speed and low light exposure, both of which are consequences of the geometry of sheet excitation and perpendicular detection (Figure 2.1b). Though the advantages of rapid imaging have been well illustrated in recent work (e.g. Refs. [7, 26]), the utility of low light levels is less apparent. Using an example from skeletal morphogenesis, in which overall shape and form develop over the course of many hours but cellular dynamics can occur at much shorter timescales, we have shown that with short exposure intervals confocal imaging can result in abnormal growth, while light sheet imaging using the same dosage of light at each imaged point allows normal morphogenesis. Notably, the phototoxicity observed during confocal imaging manifests itself as distinct trajectory though morphological space (Figure 3.5) - reflecting the lack of the widening of the opercle at the posterior end - and not simply as a slowing or delay of normal structure formation. The consequences of phototoxicity, therefore, may in general be difficult to predict, highlighting the importance of low-light-level techniques of studies of animal development. This is likely to be especially important for even higher temporal densities of data as will arise, for example, from studies mapping correlations between individual cellular dynamics and the overall development of form.

CHAPTER IV

IMAGING BACTERIAL COLONIZATION IN LIVING SYSTEMS

All plants and animals are ecosystems for microbial communities. With the advent of high-throughput "omics" technologies (including genomics, proteomics, and metabolomics) that can provide comprehensive catalogs of a microbial sample's nucleic acids, proteins, and metabolites, the stature of these under-explored and often overlooked communities is on the rise. Now that we can identify the members of these host-associated microbial communities and their functional capacities, we can ask fundamental questions about these symbiotic associations: How do particular microbial communities assemble on and within hosts? How are these communities maintained over time? How do these communities influence the development and physiology of their hosts? These questions are further motivated by human health concerns, as recent insights suggest that many diseases, including inflammatory bowel diseases, type II diabetes, colorectal cancer, autoimmune diseases, and possibly even autism are correlated with altered gut microbiota [46, 47]. A still deeper question in the field of symbiosis is the extent to which there are universal rules and mechanisms that govern the coexistence of plants and animals with thier microbial associates and whether lessons learned from model symbioses can be applied to the associations between humans and their complex microbial consortia.

Although they provide extraordinarily powerful tools for probing multi-species systems, omics approaches deliver only homogenized inventories of community

components, incapable of revealing the spatial organization and dynamics of host-associated microbial communities. To truly understand these associations, we need to be able to visualize them on the spatial and temporal scales at which microbes operate - an experimental challenge. Here we describe the application of light sheet microscopy to the field of symbiosis. In particular, we describe the utility of this imaging technique for exploring unanswered questions about the microbial colonization of the vertebrate intestine by using the model organism *Danio rerio*, the zebrafish. Hand-in-hand with omics technologies has come an explosion of data, spurring the need for analytic approaches that can make sense of information being generated about host-associated microbiota. A major thrust of these approaches is to draw correlations between the composition of a microbial community and physiology of the colonized host [48]. Analogously, large data sets documenting the three-dimensional spatial distributions of microbial and host cells over time can be analyzed to reveal spatial and temporal correlations between microbial species and between microbes and host cells to build quantitative models of microbial dynamics within a host organism.

One instructive example of insights into host colonization by bacteria comes from live imaging of the partnership between the bobtail squid *Euprymna scolopes* and the luminescent marine bacterium *Vibrio fischerii*, which colonizes the light organ of its host and provides light to erase the squid's shadow when the squid is foraging at night in shallow seawater [49]. Direct visualization of colonization using fluorescently labeled bacteria revealed host-mediated control of the microbial population, as the symbionts are selectively recruited from the seawater and collected on specialized mucus-rich external surfaces before migrating into the pores leading to the light organ [50, 51]. The squid maintains long-term control over its symbiont population by purging the contents of the light organ each dawn, thereby allowing a fresh population to regrow

from a small residual inoculum [52]. In this simple system, bacterial growth can be well described by analogy to bacterial population dynamics in a flask. An initial clonal inoculum grows exponentially until the population reaches a maximum density, and the diurnal venting of the squid is the equivalent of diluting the culture into a flask of fresh broth.

In contrast to the squid light organ, the vertebrate intestine is an open-ended tube with continual flux of microbial and dietary contents. Experimentally, researchers have attempted to model this system as a series of chemostats with climax populations of bacteria maintained at a fixed density by a continual influx of nutrients and efflux of contents [53]. In reality, we know very little about the microbial population dynamics within this organ and the extent to which the chemostat model accurately simulates the intestinal environment. For example, to what extent is the efflux balanced by regrowth of permanent residents, as in a chemostat or the squid light organ, as opposed to influx of new members from the external environment? Are there conditions that favor internal regrowth versus influx? Answers to these questions are crucial for developing treatments for human disease that minimize disturbances of gastrointestinal ecology or that maximize invasion by, for example, a probiotic. To investigate colonization of the vertebrate intestine, one needs an experimentally tractable model vertebrate that can be subject to live imaging. Ideally the host would be optically transparent, small enough for its entire digestive tract to be visualized, and amenable to microbiological manipulations, such as the ability to generate gnotobiotic animals with defined microbial associations. As discussed in previous chapters, the zebrafish larva offers all of these features, as well as a rich research history that has generated many valuable protocols and reagents for experimental manipulations.

4.1. Zebrafish as a Model for Studying Colonization of the Vertebrate Gut

Zebrafish were pioneered as a model for studying vertebrate development because of their optical transparency, rapid embryonic development, fecundity, inexpensive husbandry, and ability to be manipulated genetically and embryologically [14]. These same attributes make them extremely useful for studying host-microbe associations [54, 55]. Zebrafish first encounter microbes in their environment when they hatch out of their chorions as larvae between 2 and 3 days post-fertilization. By 4 dpf, their digestive tracts are open to the environment at both ends and begin to be colonized by bacteria in their environment. At 7 dpf, the larval stage shown in Figure 4.1, they are still optically transparent and their internal organs, including the intestine, can be readily visualized. Their *ex-utero* development enables easy derivation of germ-free, or axenic, zebrafish larvae by surface sterilization of the chorion prior to hatching [18]. Because of their fecundity and the fact that embryos can be fertilized *in vitro*, it is possible to derive thousands of germ-free fish at a time, a scale that is unobtainable in mammalian systems. Our gnotobiotic methodologies have allowed us to infer the roles that the resident microbiota play in host development by comparing the traits of germ-free and conventionally reared zebrafish [56–58]. The ability to rear germ-free zebrafish also provides a starting point for visualizing the process of colonization in real time.

Zebrafish, like all vertebrates, are colonized by complex microbial communities being found in their digestive tract. As in humans, the gut microbiota of zebrafish are dominated by a small number of bacterial phyla [59]. In teleost fish the dominant phylum is the Proteobacteria [60], which fortuitously contains the most experimentally tractable bacterial species. We and others have successfully genetically engineered a growing number of zebrafish-derived bacteria to express fluorescent proteins for

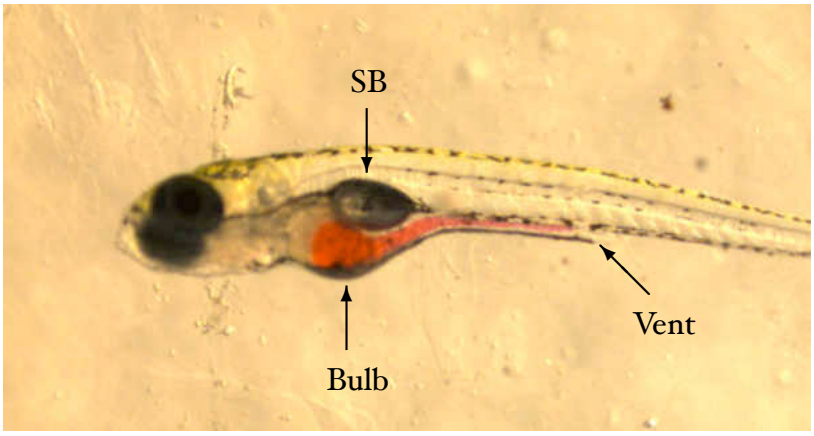

FIGURE 4.1. Five day post fertilization zebrafish larva. Phenol red has been orally gavaged and highlights the intestinal bulb, which sits below the swim bladder (SB), as well as the lower gut, extending to the vent.

visualizing their interactions with host tissues and cells. Direct visualization of infection by pathogenic in zebrafish has upended conventional wisdom about aspects of infectious disease; for example, demonstrating the dynamic nature of mycobacterial granulomas [61]. The first description of bacterial dynamics in the zebrafish intestine by Rawls and colleagues used wide-field fluorescence microscopy [62]. These authors described different types of bacterial movement in the intestinal habitat, including active swimming and passive movement of large clumps of bacteria. Their studies were, however, limited by the lack of optical sectioning and three-dimensional resolution inherent in wide-field imaging. Below we describe imaging technology that overcomes these limitations.

4.2. Zebrafish Husbandry and Bacterial Colonization

The zebrafish line *Tg-[BACmpo:gfp]* [63] (referred to as *mpo:gfp* below) was used to visualize neutrophils, and *Tg[nkx2.2a:mEGFP]* [64] (referred to as *nkx2.2a:mEGFP* below) was used to visualize enteroendocrine cells. Larvae were reared at a density of

about 1 fish/mL of embryo medium (EM) at 28.5 °C. Larvae were not fed during the experiments, instead subsisting off their egg yolks for nourishment. Embryos from natural or *in vitro* fertiliization crosses of wild-type AB/Tu fish were derived germ-free as described in [18]. Germ-free larvae were inoculated with bacteria at 3 dpf, unless otherwise noted. Larvae were removed from flasks with bacteria, rinsed once in sterile EM, and anesthetized in MS222 (tricaine methanesulfonate), then mounted in agar prior to imaging in the light sheet microscope. Anesthetized fish could be maintained for up to 24 hours of continuous imaging. Viability of the fish was assessed by the beating of the heart and the occurrence of peristalsis in the intestine. We observed, as has been previously noted [65], that older larval fish were more susceptible to MS222 toxicity, so we employed doses no higher than 80 mg/L and larvae no older than 6 dpf.

4.3. Visualizing Bacterial Colonization Dynamics in the Zebrafish Intestine

To begin to investigate bacterial colonization dynamics in the zebrafish intestine using light sheet microscopy, we performed experiments in which we inoculated initially germ-free larvae with fluorescently labeled *Aeromonas veronii*, a common bacterial resident of the zebrafish intestine, and imaged them over an extended time period. We incubated the fish with the bacteria for 6 hours prior to imaging, which was the shortest inoculation time that ensured consistent colonization across all of the fish. *A. veronii* colonization of the germ-free intestine could occur by many possible mechanisms. In one extreme model, a single bacterial cell could colonize the organ and clonally expand. A second model, at the opposite extreme, would involve continuous influx and efflux of bacterial cells, with no growth occurring within the intestine itself. A third model, commonly evoked in the human gastrointestinal literature, posits that

microbial growth in the intestine resembles growth in a chemostat [53], with bacterial cell proliferation being driven by influx of nutrients into the system and balanced by efflux of contents out of the system. To discriminate between these and other possible colonization dynamic models, we simultaneously exposed germ-free zebrafish larvae to two isogenic strains of wild type *A. veronii* with similar *in vitro* growth rates, one expressing green fluorescent protein (HMTn7GFP) and the other dTomato (HMTn7RFP). The larvae were incubated with the bacterial strains for 6 hours, after which three-dimensional images spanning the entire intestine were collected every 20 minutes for 18 hours. Each three-dimensional data set, roughly 3 GB in size, was obtained in approximately 60 seconds per color channel.

In all fish examined, we observed both fluorescently marked *A. veronii* strains within the zebrafish intestine (Figure 4.2a)., ruling out the first model of colonization by a single cell. The second model of continuous influx of bacteria from the environment without population growth in the intestine was also not supported by our data. In media in which the fish were inoculated, we observed a well-mixed distribution of red and green members (Figure 4.2a). The pattern of multicolored clumps of cells is expected because the cells are genetically identical except for the fluorescent proteins they produce and thus should have no bias for homotypic aggregation. In contrast, in the fish intestines, we observed single-colored aggregates of cells, which we interpret to occur through clonal expansion of single cells (Figure 4.2b-j). We speculate that some of the larger clumps consist of clonally expanded cells adhering in biofilms to flocculent material such as host mucus or dead cells shed from the intestinal epithelium [66]. Interestingly, some of these clumps persist for a long time, others transit through the intestine rapidly, while still others disintegrate or become dislodged from formerly stable locations, indicating that the fluid dynamics within this organ are extremely

complex. The heterogeneous distribution of clumps of bacterial cells we observed was also inconsistent with the model of a well-mixed chemostat, although more complex models of unmixed chemostats could apply [67].

The light sheet microscope allows us to monitor bacterial population abundance and dynamics in real time in the zebrafish intestine. Some of the fluorescent signal observed emanated from the fish tissue itself, as is apparent when we image germ-free animals or animals colonized with low numbers of bacteria. Certain host cells of unknown identity emit very bright autofluorescent signals, but these are easily distinguished from colonizing bacteria because of their large size, their position outside of the gut lumen, and the fact that their autofluorescence is detected in both the red and green channels. The intensities of red and green fluorescence within the intestinal lumen, above a threshold intensity applied to remove low-level fluorescent background, correlates fairly well with the relative abundance of red and green-labeled cells, as measured by dilution plating ([68]), validating our use of fluorescence intensity as a surrogate for bacterial population size and location. In contrast to a chemostat in which the entire volume is occupied by microbial cells utilizing available resources to support their growth, our imaging of the zebrafish intestine revealed bacterial colonization to be spatially highly heterogeneous, with punctate colonies and nonuniform distribution of colonies along the length of the gut (Figure 4.2b-j). Additionally, the spatial distribution of bacteria was highly dynamic, with large changes in overall abundance as well as localization occurring during the imaging period (Figure 4.2c-j). Our observations support two possible models of the intestinal environment, which are not mutually exclusive: first that resources for bacterial growth are distributed non-uniformly and highly dynamically in the zebrafish intestine; and second that other determinants, such as peristaltic forces or immune cell surveillance, play significant roles in bacterial

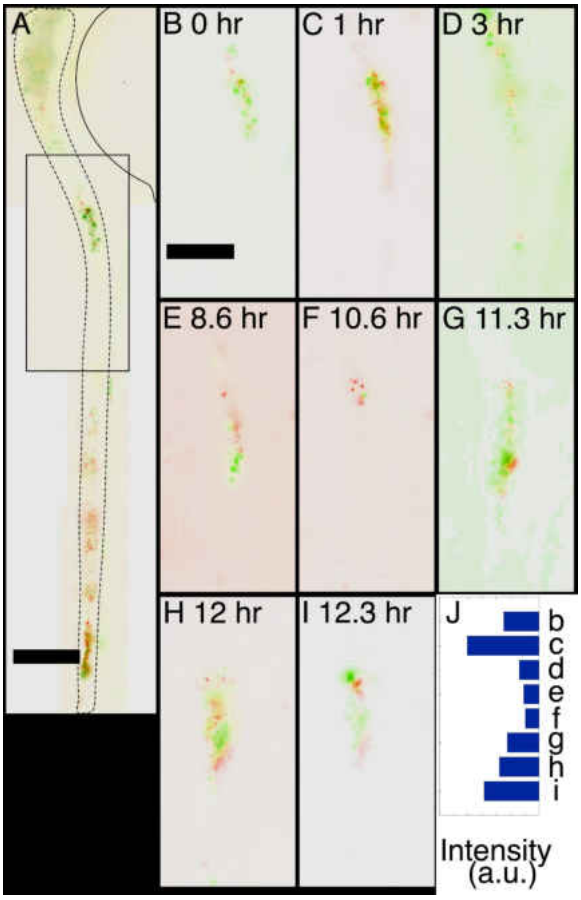

FIGURE 4.2. Colonization of a larval zebrafish gut by GFP-expressing and dTomato-expressing *A. veronii* bacteria (fluorescence image, background inverted for clarity). (A) Wild type GFP-expressing and dTomato-expressing *A. veronii* co-inoculated in culture. Panels B-J show representative two-dimensional optical sections from 3D data sets. (B) The entire gut 6 hours after inoculation. The gut is approximately outlined with a solid line. (C-J) The distribution of the two microbial populations in the region corresponding to the box in (B) at various times after inoculation, with t = 6 hrs. corresponding to panel B. The contrast of each panel was independently adjusted so that the bacterial populations are clearly visible despite fluctuations in overall bacterial abundance. In each panel, both red and green intensities were rescaled by the same amount. (K) The intensity rescaling factor in each of panels (B-J) - that is, the sum of the red and green intensities each normalized by the typical brightness of a typical bacterium, providing a measure of the total bacterial abundance at each time. Scale bars: (A) 10 μm; (B-J) 100 μm.

population distributions. It is clear that the simple model of a chemostat with evenly distributed bacterial cells does not accurately describe populations in the zebrafish intestine.

The high speed of light sheet fluorescence imaging also enables observations of the motility of individual bacterial cells. Supplemental movie S1 in [68] shows a two-dimensional section of a larval zebrafish intestine with dTomato-labeled *A. veronii* bacteria (HMTn7RFP) (as in Figure 4.2). Several distinct motility patterns are evident, including bacteria in stationary clumps, bacteria passively moving with the fluid flow, and bacteria that are actively swimming. While motility is relatively straightforward to study *in vitro*, its properties *in vivo* are largely unexplored and may not reflect those of cultured bacteria due both to the complex physical environment of the intestine and to signaling among intestinal constituents. Future analyses of bacterial cell dynamics in the zebrafish intestine will investigate how individual cells explore their local chemical and spatial environments, what proportion of the community are permanent residents as opposed to transients, and whether motility is a prerequisite for permanent residency. *Aeromonas* species are of particular interest, as they have been shown to exhibit chemotaxis toward fish mucus [69] and to engage in different modes of motility mediated by different types of flagella [70].

4.4. Visualizing Host Cell Dynamics in the Intestine

An important question in the field of symbiosis is how the process of colonization and the presence of microbial associates change the development and function of the host. We have characterized numerous zebrafish traits that are affected by the microbiota. For example, germ-free zebrafish intestines have a paucity of secretory cells, including enteroendocrine cells, which secrete hormones, and neutrophils, which

are phagocytic cells of the innate immune system [56, 57]. In addition, the physiology of the intestine is altered in the absence of the microbiota, with more rapid peristaltic contractions [56]. The high speed of light sheet microscopy provides an opportunity to explore host-microbe interactions at much higher resolution and to ask how the microbiota affect the dynamics of individual zebrafish cells, and reciprocally, how host cells affect the microbiota.

To demonstrate the feasibility of this approach, we used the transgenic zebrafish line *nkx2.2a:egfp*, which drives expression of a membrane-bound GFP in enteroendocrine cells in the intestinal epithelium [64]. Six days post fertilization larvae were imaged for several hours (Figure 4.3a-g), demonstrating the ability of future in-depth studies to follow the genesis of these cells in the presence and absence of microbiota. Imaging also shows the dynamics of these cells and emphasizes the extent to which they experience mechanical forces during the propulsion of perstaltic waves along the length of the intestine; distortions of cell shape are clearly visible during such a contraction (Figure 4.3a-f). Typical image acquisition timescales, roughly tens of milliseconds for two-dimensional slices and a few seconds for three-dimensional images, are faster than the periodicity of peristalsis, allowing imaging without motion-induced blurring. Since there are fewer of these cells in the germ-free intestine, and since they produce hormones that regulate peristalsis, we expect to observe interesting changes in the cellular and organ-wide contractile behaviors during colonization.

In addition to the cells of the intestinal epithelial, gut microbes interact with immune cells that actively survey this tissue. Neutrophils are important first responders to intestinal infections, and we have shown that these cells are also recruited to the intestine upon colonization by the microbiota [57]. Being highly motile and responsive to chemical cues, neutrophils are a model cell for chemotaxis studies, and their *in vivo*

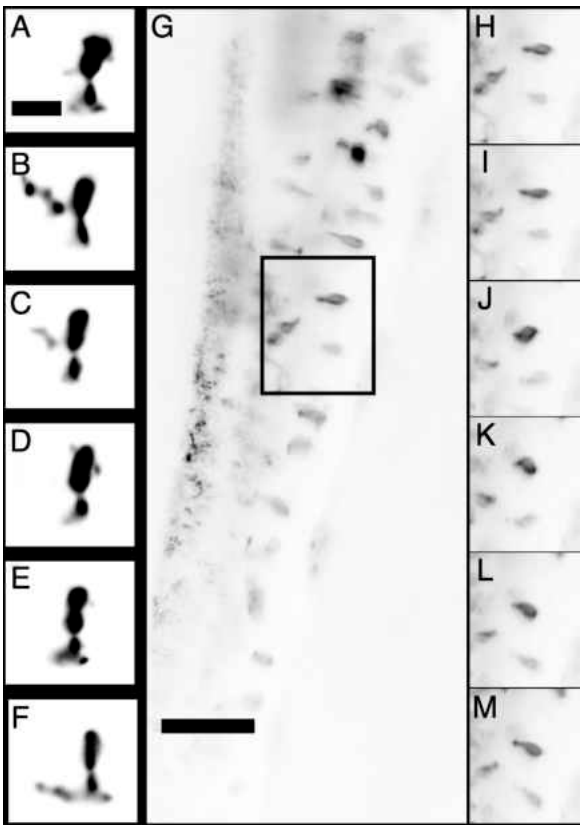

FIGURE 4.3. (A-G) Fluorescently labeled enteroendocrine cells (transgenic line *nkx2.2a:egfp*, intensity inverted for clarity) in a larval zebrafish gut. Scale bar: 40 μm. (A-F) A time series of the cells within the box in (G). The interval between each panel in (A-F) is 2.8 s. The deformation and movement of cells as the gut undergoes peristalsis during the imaging period is evident. The movie from which these images were taken is provided as Movie 2 in (http://www.biolbull.org/content/223/1/7/suppl/DC1). (H-M) A single fluorescently labeled neutrophil (*mpo:gfp*) within the intestinal tissue of a larval zebrafish. Each panel is a two-dimensional optical section from a three-dimensional data set, each separated in time by 2 minutes. Dynamic rearrangements of the neutrophil's filopodia are evident. Scale bar: 10 μm.

behavior has been characterized extensively in zebrafish by using confocal microscopy (e.g. [71–73]). Visualizing their dynamics in internal tissues such as the intestine, however, poses technical challenges that we were able to overcome using light sheet microscopy. We visualized GFP-labeled neutrophils in the *mpo:gfp* transgenic line [63] at various stages from 4-8 dpf in time-lapse scans of the whole intestine for several hours. We obtained scans spanning 60 μm thick intestines with optical slices separated by 1 μm in as little as 12 seconds per three-dimensional data set. The speed and range of imaging allowed us to identify neutrophils undergoing active processes at different depths throughout the intestine, and we were able to visualize individual cell shape rearrangements such as the extension and retraction of filopodia (Figure 4.3h-m). Simultaneously imaging fluorescently labeled bacteria and neutrophils with light sheet microscopy will enable visualization of neutrophil recruitment to the intestine upon bacterial colonization and will address whether they exhibit different behaviors, such as increased filopodia activity, in the presence of commensal microbes. By examining correlations between local heterogeneities in the microbiota and the positions of neutrophils, we will also be able to explore the possibility that neutrophils influence bacterial population growth dynamics.

4.5. Analyzing Cell Population Dynamics *in vivo*

Live imaging of intestinal bacteria with high spatial and temporal resolution over hours or days produces a vast quantity of image data. The two-color imaging of gut microbes illustrated in Figure 4.2, for example, yielded over 300 GB of images from a single larval zebrafish; this number could easily be increased with finer temporal sampling or a greater number of labeled populations. Like other recently developed biological techniques, such as high-throughput sequencing and proteomic methods,

light sheet imaging shares the challenge of extracting comprehensible insights from high volumes of data. It is likely that a variety of approaches to this task will be developed as data sets become available. We suggest here a few promising perspectives.

As a pre-requisite to utilizing the full three dimensional nature of colonization image data, simply counting the total number of bacteria present in the gut can result in useful insights into the ecology of the system. In order to accomplish this task, we make use of custom written software capable of robustly identifying both individual cells, as well as aggregates, converting fluorescence intensity into population size. This course-grained data (as shown in Figure 4.4) is ideal for testing mathematical models of population dynamics. For a single species (*A. veronii*) colonization of a larval zebrafish,

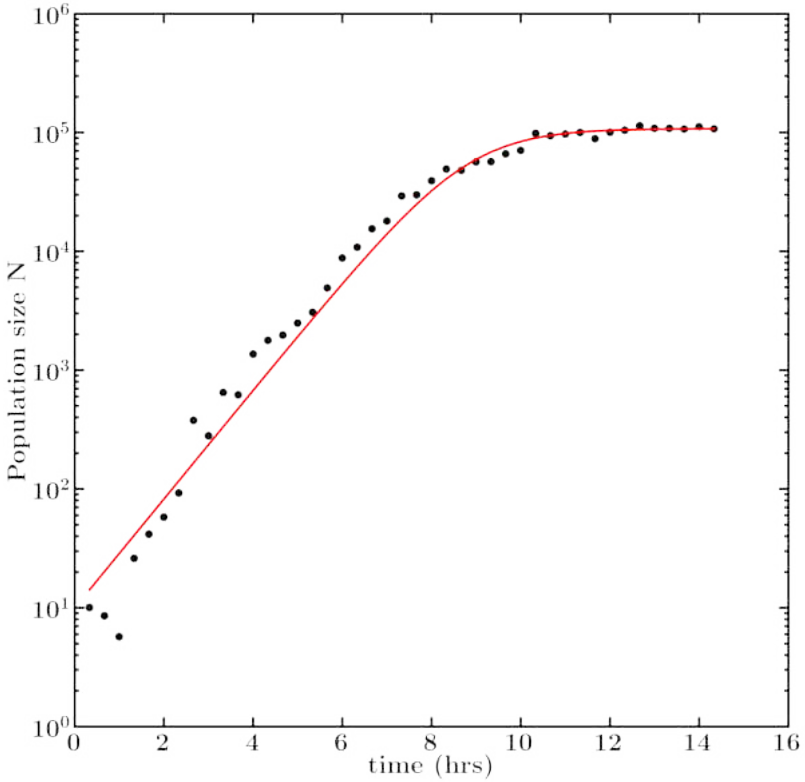

FIGURE 4.4. Representative plot of bacterial population obtained from image data of *A. veronii* colonizing a larval zebrafish gut over ≈15 hours. The solid line is a fit of the data to equation 4.2 and time is from the beginning of imaging.

this data is remarkably consistent with the logistic growth equation:

$$\frac{dN}{dt} = \kappa N\left(1-\frac{N}{K}\right) \tag{4.1}$$

$$N(t) = \frac{KN_0\exp[\kappa t]}{K=N_0\left(\exp[\kappa t]-1\right)} \tag{4.2}$$

which models a population N with a constant growth rate κ and access to a finite amount of resources, leading to a steady state carrying capacity K. We find this behavior to be robust across many fish, with $\langle\kappa\rangle = 1.3 \pm 0.3$ hr^{-1} for single species colonization of *A. veronii* (five samples, mean $\pm$ standard deviation).

Although it is instructive to look at the integrated number of bacteria populating the gut, the raw data output by light sheet imaging of fluorescently labeled microbes denotes the density of bacteria over time *and* three-dimensional space. A simple distillation of this information is provided by collapsing this density onto the axis provided by the gut itself, integrating the intensity of image slices perpendicular to the gut center-line at each point along the line and yielding a one-dimensional measure of bacterial population along the anterior-posterior coordinate. This one-dimensional projection can be performed for each measurement time, as illustrated in Figure 4.5 for the data set from which Figure 4.2 was extracted. From this and other observations, it is evident that bacterial populations are not homogeneously distributed along the gut. One can correlate the existence of preferential locations for bacterial growth with anatomical position, noting, for example, high population density in the most anterior and posterior regions of the intestine. Moreover, it is evident that the dynamics of growth are complex; the spatially nonuniform distribution present initially is not simply scaled or magnified as time progresses, but rather varies non-monotonically over the course of hours.

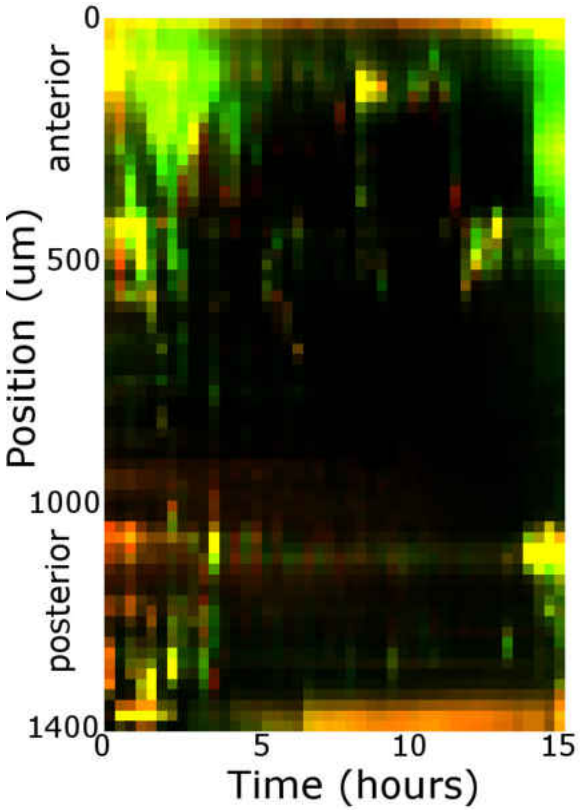

FIGURE 4.5. Population distributions as a function of time for the two co-inoculated bacterial populations illustrated in Figure 4.2. Each column indicates fluorescence intensity integrated over the dimensions perpendicular to the gut axis, providing a one-dimensional measure of bacterial density along the gut, the temporal dynamics of which can be visualized in a two dimensional plot.

While projections are easily comprehensible, they necessarily neglect three-dimensional structure and dynamics. Considering interacting bacterial species, it will likely be fruitful to investigate spatial correlation functions that involve different microbial groups. Co-localization, anti-localization, and spatially offset population densities can reveal the functional relationships between species that cooperate, compete, or interact *via* exchange of metabolites. Moreover, correlation functions can provide a measure of structure that maps higher-dimensional organization onto visualizable lower-dimensional spaces.

To illustrate this, we first consider the schematic, computer-generated imaged in Figure 4.6a, in which green spots are distributed randomly in two dimensions, and slightly larger red spots are positioned such that each is some particular distance (here, 20 ± 1 pixels) from a green spot, in a random direction. By construction, the correlation between red and green is not perfectly sharp. For each green spot, there is a red spot placed 20 ± 1 pixel away. This red spot may be less than or greater than 20 pixels distant from other green spots. This correlation between the red and green structures in Figure 4.6a is not apparent by eye. Denoting the intensity of pixels in the green and red channels I_g and I_r, respectively, the normalized cross-correlation is given by Gonzalez and Woods [74]:

$$C_g r\left(\vec{\rho}\right) = \frac{\Sigma\left(I_g\left(\vec{r}\right) - \langle I_g \rangle\right)\left(I_r\left(\vec{r} - \vec{\rho}\right) - \langle I_r \rangle\right)}{\sqrt{\Sigma\left(I_g\left(\vec{r}\right) - \langle I_g \rangle\right)^2 \Sigma\left(I_r\left(\vec{r} - \vec{\rho}\right) - \langle I_g \rangle\right)^2}} \tag{4.3}$$

where $\vec{r}$ indicates position, $\vec{\rho}$ is the spatial offset, $\langle\ \rangle$ indicates the average over pixels, and the sums run over all pixels in an image. If the two intensity distributions are spatially offset by some well-defined amount, the numerator in the above expression will be large when $\vec{\rho}$ equals that amount, and C_{gr} will have a peak at that offset. This

is evident in Figure 4.6b, which shows $C_{gr}\,(\vec{\rho})$ for the image in Figure 4.6a, yielding a ring at a displacement of 20 pixels from the origin. In Figure 4.6c we show $C(\rho)$, the correlation as a function of radial displacement $\rho = \|\vec{\rho}\|$, that is, averaged over angle. Again, a 20-pixel offset is apparent.

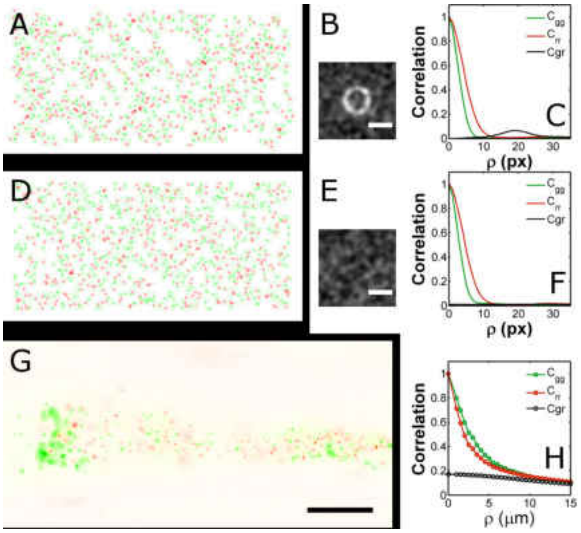

FIGURE 4.6. Image auto- and cross-correlations (background intensity inverted for clarity). (A) A simulated two-dimensional image with randomly positioned green spots and 1.5 $\times$ larger red spots each placed about 20 pixels from a green spot, randomly oriented. (B) The two-dimensional cross-correlation, C_{gr}, of the green and red channels of (A); a ring at a radius of 20 pixels reveals the constructed correlation. (C) The radial dependence of the auto- and cross-correlation functions; as in (B), C_{gr} shows a peak at a spatial offset of 20 pixels. (D) A simulated two-dimensional in which both green and red spots are positioned ranomly. (E, F) The correlation functions corresponding to the image in (D). (G) A single optical slice from a three-dimensional data set depicting *Aeromonas veronii* bacteria in a larval zebrafish, as in Figure 4.2, at a single time point. Scale bar: 50 μm. (H) Auto- and cross-correlations of the bacterial intensity distributions calculated from the three-dimensional data set.

Particular coordinate systems can help characterize particular spatial distributions of bacterial populations. For example, by determining the gut center line (either manually or by computational analysis of the bounded space), one can define a cylinder-like coordinate system, the radial component of which distinguishes luminal and

mucosal positions in the gut. Considering cross-correlations in which $\vec{\rho}$ is the radial coordinate, situations in which one population is predominately mucosal and the other is predominantly luminal would give a peak in C_{gr} at some radial displacement.

The auto-correlation of each intensity function (i.e. its correlation with itself) also provides useful informaiton. $C_{gg}\left(\vec{\rho}\right)$ and $C_{rr}\left(\vec{\rho}\right)$ each trivially have a peak at $\vec{\rho} = 0$, as any function is perfectly correlated with itself; these autocorrelations decay with a characteristic scale equal to the typical object size in the intensity images. We see this decay in Figure 4.6c; as expected, the red autocorrelation curve has a larger decay length, as it corresponds to the larger particle size.

In contrast, Figure 4.6d-f shows simulated images and the resulting calculated correlations for images in which the position of both the red and green spots were completely random. For such distributions, the cross-correlation has a low, featureless value.

We provide an example of correlation function analysis of real three-dimensional bacterial images in Figure 4.6g & h. The source data are from the same setup as illustrated in Figure 4.2: two-color images of *A. veronii* HMTn7GFP and HMTn7RFP in the intestine. The intensity correlations shown in Figure 4.6h are calculated from a 166 $\times$ 333 $\times$ 64 μm^3 volume at a single time point, one optical section of which is depicted in Figure 4.6g. The autocorrelations are similar in each color channel with a characteristic length-scale of a few micrometers. The cross-correlation is small and featureless, as expected, as these two populations are biologically identical and should be randomly situated.

More generally, we can expect different sorts of correlations from more complex sets of species, and a key goal of the present work is to encourage progress along these lines. A lack of cross-correlation near $\vec{\rho} = 0$, for example, can indicate competing

species that are unlikely to occupy the same spatial niche. Strong correlation at some non-zero distance can reveal, for example, cooperating species whose interactions are mediated by the exchange of metabolic products whose dispersal spans some characteristic range. Of course, using cross-correlations to compare groups requires assessment of the precision of multicolor image registry, which can be compromised by both optical aberrations and by motions of the specimen. Control images can be provided, for example, by larvae that have ingested multicolor fluorescent beads, the images from which should be perfectly correlated. The use of autocorrelations to determine typical colony sizes requires no such multicolor registry, and in itself can reveal features of importance such as growth of typical colony sizes with time.

It should also be possible to use characterizations of bacterial motility, enabled by the high speed of light sheet microscopy, to examine spatial correlations between differently motile groups. Using either temporal correlations between images or direct tracking of moving microbes, bacterial populations with the same fluorescent reporters can be divided into categories of different motilities, and spatial correlations between these subpopulations could be examined using the same approach described above. We expect that such studies may illuminate connections between microbial behaviors and gut colonization.

4.6. Discussion

Advances in genomics, proteomics, and metabolomics have generated an explosion of information about bacterial associations of humans [48]. This flood of data is enabling new approaches to modeling the metabolic activities and ecological interactions of host-associated microbial communities (e.g. [75, 76]), which will enrich the entire field of symbiosis. These approaches, however, are based on samples that

are homogenized mixtures of microbes at a single point in time, and they fail to take into account the complex spatial dynamics of microbial populations [77],

The study of spatial population dynamics has a long history in ecology [78], but the application of these ideas to naturally occurring microbial communities has been hindered by the technical challenges of observing population dynamics on the spatial and temporal scales of microbes. Here we present the methodology of light sheet microscopy and its application to visualizing the dynamics of zebrafish intestinal microbiota and associated host cells. The spatial resolution and nondestructive sampling of light sheet imaging will provide researchers with new opportunities to apply ecological theories and concepts to the study of host-associated microbial communities.

Four-dimensional imaging will afford the opportunity to study the colonization and succession of gut microbial communities [79], determining where in the intestine microorganisms first establish and how this influences the ability of successive colonizers to invade. The mechanisms that drive and control the population dynamics of bacterial species (e.g. dispersal, trophic interactions, environmental pressures) can be inferred by examining patterns of the synchrony of populations across space and time [80]. Further questions that can be illuminated with this technology include whether succession is driven more by expansion from initial colonizers or from continued migration, how communities respond to disturbances (secondary succession), and where these dynamics occur with relation to host cells and landmarks. Light Sheet imaging is particularly useful for visualizing the dynamics of symbiosis in live animals because of the speed of image acquisition and the low photodamage. Light sheet imaging could be employed to image microbial colonization of the internal organs of transparent animals, including marine organisms and insect larvae, and to record

bacterial associations of surface tissues of any animal or plant. We speculate that it will be especially powerful when applied to model symbiosis systems of bacterial associations such as the squid light organ, the leech crop, the fruit fly and nematode digestive tracts, and fungal and bacterial interactions with plant roots and rodent skin.

Here we have presented results that demonstrate the feasibility of using light sheet imaging to characterize the bacterial colonization of the zebrafish intestine and the host's response to this colonization at a resolution that informs us about the behaviors of individual cells and the dynamics of entire populations of cells. We discuss the challenges of making sense of the vast amounts of image data generated by this four-dimensional microscopy and present approaches to analyzing and interpreting correlations between different simultaneously imaged cell populations. An important future goal will be to integrate other types of "omics" data with *in vivo* imaging of host-associated microbial communities. Although this will be a formidable challenge, we believe that taking into account spatial organization and temporal dynamics of complex microbial communities resident on animals will be essential for understanding these communities' metabolic activities and the causes and consequences of those activities. In comparison to all other bacterial communities sampled across the globe, the communities found with the vertebrate intestine have a unique phylogenetic composition [81]. We suspect that vertebrate intestinal microbiota will also posses unique spatial organizations and temporal dynamics that cannot be approximated by models such as the chemostat, which fails to take into account the complex reciprocal interactions between the microbes and their host environment. Direct visualization of these microbe-host interactions is the first important step toward understanding the growth, development, and function of these microbial communities that are integral to animal biology.

CHAPTER V

MAGNETIC BEAD MICRORHEOLOGY

Biological systems provide a wealth of complex and interesting materials, the physical properties of which are important not only to the organisms to which they belong, but also to commensal and pathogenic organisms that may occupy a living host. While many biological materials may be well characterized *in vitro*, doing so necessitates altering the living system at best, and destroying it at worst; certain biomaterial properties would benefit from being measured within the full biological context of their natural environment.

The rheology of a material - how it deforms and flows - can depend on the length, time, and shear scales on which it is probed. In a biological system, it may mature over time, vary in space, and respond to biophysical, biochemical, and genetic stimuli. Additionally, such biological materials are often only present in quantities too small to probe with traditional techniques and may be far from thermodynamic equilibrium. It is therefore important to develop new methods for studying the rheology of materials on scales relevant to biological systems, and as a result the field of microrheology has grown to provide many techniques [82–84] which have been applied to a wide variety of systems. Many systems of interest, however, are still resistant to study with existing microrheological methods.

In the previous chapter, the importance of an animal's microbiome was discussed and a method to monitor its organization and time evolution was developed. Although there is much to be learned from such studies of the composition and behavior of the constituent bacteria, one must not forget that they are themselves part of a larger system that includes the host environment. New insights into this system may be gained by developing experimental techniques which can simultaneously probe the

constituent members of bacterial colonization, physiological condition and behavior of host cells, and the mechanical nature of the internal environment. It is the aim of this chapter to develop a microrheological technique that can be integrated with emerging methods for studying the dynamics of bacterial colonization in animals, namely the methods of chapter IV.

The material of interest here is mucus, a substance consisting of glycoproteins that is ubiquitous throughout many organs of animals and that can have physical properties that vary over many orders of magnitude [85] depending on, for example, the health of the animal. In particular, we study the gastrointestinal mucus of the zebrafish, guided by the knowledge that in humans, the gut is home to the largest portion of the microbiome [86]. There are many good reasons to measure the viscosity of intestinal mucus *in vivo*, foremost of which is that such a measurement *in vitro* would require the careful extraction of mucus from the fish's intestinal bulb, which contains perhaps a few nanoliters of material. Furthermore, in order to use traditional rheological measurement tools, a sample size of 0.10-1.0mL is needed, which would necessitate the removal of gut contents from 10^5-10^6 fish, a daunting task to consider. An additional benefit of performing an *in vivo* measurement is the possibility to monitor changes in response to biological stimuli. For example, it has been shown that bacteria can alter the properties of mucus both directly, by chemically modifying it [87], and indirectly, by manipulating the host cells that are responsible for its production [56]. For all of these reasons, I set out to develop a measurement tool that could be used to characterize the material response of intestinal mucus, at the length scale of bacteria, in a non-invasive manner suitable for observing changes over time and throughout the spatial structure of the larval zebrafish gut.

5.1. Theoretical Background and Experimental Design

Because the larval zebrafish gut undergoes peristalsis, and can therefore create bulk fluid flow, I chose to forego passive microrheology techniques (which rely on thermal diffusion) in favor of an active measurement. In active microrheology, external forces can be applied to micron scale probes, whose response in turn reveals the mechanical nature of the surrounding material. Such external forces can be generated using, for example, optical traps, atomic force microscopes (AFM), or magnetic fields [82]. The least invasive method would be to use a magnetic field, which leaves biological tissue unaffected, the field passing through it without distortion. Generating a magnetic force on a magnetic dipole, however, requires the establishment of a magnetic field *gradient*, which would be difficult over the length scale of interest here (namely a few microns). I therefore chose to apply an external magnetic torque, which can arise from a uniform field, the vector orientation of which can be easily controlled externally. By using fluorescent polystyrene microspheres which are rendered superparamagnetic by doping with grains of magnetite (Spherotech FCM-4052-1), I will have a bright probe particle that is readily visible and localizable in three dimensions in the light sheet fluorescent microscope. The fact that they are superparamagnetic essentially means that they will have a strong magnetic response that rapidly saturates to a constant value and has no hysteresis.

To understand how a magnetic torque on an object can be used to measure its surrounding environment, I first consider the case of a Newtonian fluid, whose constitutive law is given by the equation $\sigma = \eta\dot{\gamma}$, where σ is the applied stress, η is the fluid's viscosity, and $\dot{\gamma}$ is the time rate of change of the strain in the material. In this case, the stress will arise from the torque applied by the external field, given by $\vec{\Gamma} = \vec{m} \times \vec{B}$, $\vec{m}$ being the induced magnetic moment of the particle and $\vec{B}$ the

external field. The strain in the material will be reflected by the orientation of the particle, which I will denote as θ (see Figure 5.1b). The constitutive law may be re-written in terms of the torque and particle orientation as $\Gamma = \eta\xi\dot{\theta}$, where ξ is a function that contains geometrical factors necessary to make the correspondence between stress/torque and strain/angle. If the magnetic field is rotated in an oscillatory manner, such that the angle takes the form $\beta = \beta_0 \exp(i\omega t)$, the particle orientation will also oscillate at the same frequency, but with a different amplitude and phase $\theta = \theta_0 \exp(i\omega t + \phi)$. These functional forms may be used in the constitutive law to yield a relationship between the orientation of the field and probe particle:

$$\begin{aligned} \Gamma &= \eta\xi\dot{\theta} \\ mB\sin(\theta-\beta) &= \eta\xi i\omega\theta \\ mB(\theta-\beta) &\approx \eta\xi i\omega\theta \\ \theta_0 &= \beta_0\sqrt{\frac{1}{1+(\omega/\omega^*)^2}} \qquad (5.1) \\ \phi &= \arctan\left(-\frac{\omega}{\omega^*}\right) \qquad (5.2) \end{aligned}$$

where the small angle approximation has been used for the difference between β and θ and the characteristic frequency is defined as $\omega^* \equiv mB/\xi\eta$. Since a Newtonian fluid has only dissipative response, it may be obtained via either the frequency dependent amplitude or phase response of the particle. More generally, for the case of an oscillatory stress and strain, the constitutive law is given by $\sigma = G^*(\omega)\gamma$, where the complex shear modulus $G^* = G' + iG''$ contains information about the storage and loss moduli via its real and imaginary components. For the current discussion, I simply note this for completeness and return to considering the Newtonian case.

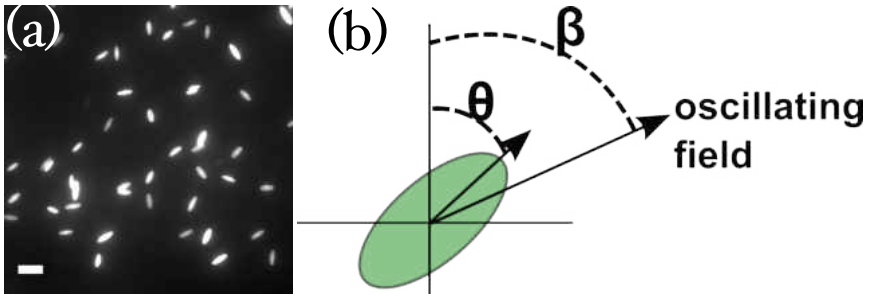

FIGURE 5.1. (a) Fluorescence image of elongated magnetic microspheres (scale bar is 10μm). (b) Definition of angles θ and β.

5.1.1. Magnetic Bead Elongation

Measuring the orientation of a microscopic probe particle is impossible if it is spherically symmetric. Therefore, to facilitate the visualization of the oscillatory motion needed to fit Equation 5.1, I deform the magnetic particles by mechanically stretching them into prolate spheroids with their magnetic moment aligned with the major axis. The general strategy is outlined in [88, 89]. First, a preparation consisting of 7% polyvinyl alcohol (PVA) and 2% glycerol (by weight) is poured onto a clean glass surface. Next, 40μL of bead stock solution is added to 1.0mL of the polyvinyl alcohol solution, mixed using a vortex mixer, and sonicated for several minutes to break apart any aggregated beads. This is then added to the middle of the previously poured solution and allowed to dry overnight into a thin film. Once the film can be removed from the glass plate, it is placed under slight tension on a mechanical stretching device and submerged in a toluene bath for 3 hours. The toluene acts as a solvent for the polystyrene, partially dissolving the beads while leaving the vinyl film intact. Tension is applied with the mechanical stretcher in one direction until the film is stretched to twice its original length, distorting the particles into prolate spheroids. Now removed

from the toluene, the film is allowed to dry for several hours so that the particles re-solidify, locked into their new shapes.

Dissolving the PVA into water allows the recovery of the ellipsoidal particles by centrifuging the particles out of solution and exchanging the supernatant with water several times. This process is observed to leave the fluorescence of the particles viable and to result in prolate spheroids with the easy axis of magnetization aligned with the major axis.

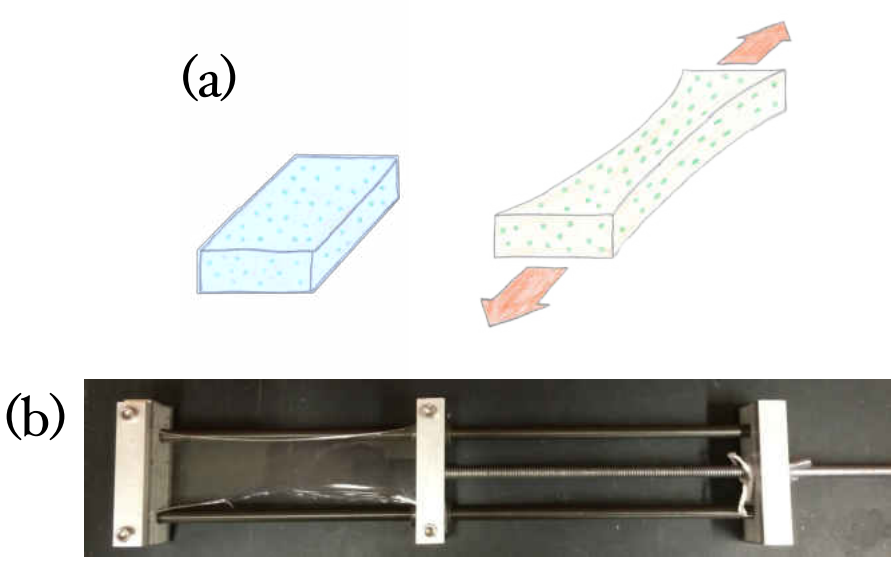

FIGURE 5.2. Elongation of polystyrene microspheres. Beads embedded in a polyvinyl film are elongated into prolate spheroids as the film is stretched (a). Stretching apparatus, with film is shown in (b).

5.1.2. Experimental Apparatus

My experimental setup, as shown in Figure 5.3, consists of a pair of neodymium magnets oriented such as to create a permanent uniform magnetic field directed vertically in a volume where the sample is located (field of view roughly 400×300 μm^2). Additionally, a ferrite core electromagnet is mounted to one side of the sample

such that, when supplied with a current, the orientation of the field is tilted to an angle β with respect to vertical. This is contained within the sample chamber of the light sheet microscope (described in chapter II) such that the excitation laser enters from the side opposite the electromagnet, allowing the generation of an oscillating magnetic field whose vector orientation lies within the imaging focal plane. This field

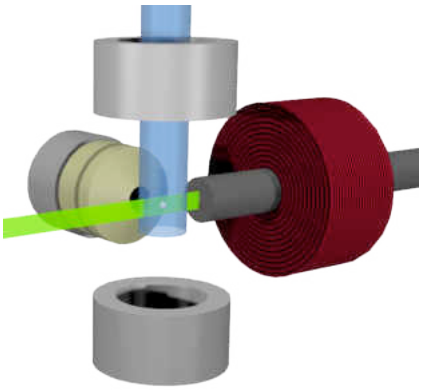

FIGURE 5.3. Schematic of magnetic apparatus inside the light sheet microscope. Upper and lower rings are permanent neodymium magnet with their moments facing vertically. A ferrite core electromagnet is on the right side, opposite the laser excitation sheet (green).

may be stepped through a progression of different frequencies in order to measure the response and then fit to Equation 5.1 or 5.2 to extract the viscosity η of the surrounding fluid. An additional strategy, which may be employed when data must be collected fast over a large range of frequencies (e.g. within the zebrafish gut between peristaltic waves), is to chirp the input signal such that it has a continuously changing frequency that covers the range of interest. The analysis of raw image files, and the subsequent time-dependent data sets using these two methods will be discussed next.

5.1.3. Data Analysis

The first step is to extract from each frame of video the instantaneous orientation of the elliptical particle. Because the particles are large compared to the resolution limit of the microscope, this step requires only very basic image processing and is implemented using custom software utilizing the OpenCV library for C++, which has functions for all of the necessary operations [90]. Briefly, an image is contrast-enhanced by making use of the morphological top hat and bottom hat transformations. Next, the image is morphologically closed and then opened in order to reduce the number of falsely identified objects by eliminating small scale structure. The grayscale image is then transformed into a binary mask by thresholding, using the Otsu method. OpenCV's `findContours()` function then yields the particle's angle (θ), width, length, and center of mass. These values, in addition to the time stamp provided by the camera, are outputted to a text file which is easily accessed for further analysis Depending on the image size, this code can be very fast ($\approx$ 10 ms per frame including hard drive read time), and can therefore be run in "real time," eliminating the necessity to store raw image files, though for the work described here, all images are saved and subsequently analyzed.

This data, representing $\theta(t)$, is further analyzed using custom Python code [91]. If the driving frequency was incrementally stepped through a series of constant values, a simple Fourier sine and cosine decomposition can recover the amplitude and phase of the signal (see Figure 5.4). If instead, the driving frequency was chirped through a continuous range of frequencies, a different method must be employed. The short-time Fourier transform is one such method, which simply computes the Fourier transform within a sliding, time-limited window in order to yield a time-dependent spectrum of the signal. This transform, however, has many undesirable qualities. For example, the

resolutions it can achieve in frequency and time are inversely related: one gains time resolution at the expense of frequency resolution and *vice versa*. Also, the short-time Fourier transform does not preserve the marginals of a distribution. This means that if one has computed the power spectrum $P(f,t)$ and wants to recover $P(f)$, it cannot be obtained by integrating over time: $P(f) \neq \int P(f,t)dt$. This arises from the fact that the windowing function, used to gain time resolution, corrupts the signal [92]. A better method utilizes the pre-existing knowledge of the input signal and is common in the field of electrical engineering.

The input and output of a linear, time-invariant system (e.g. $\beta(t)$ & $\theta(t)$), can be related in frequency space via the system's *transfer function*: $\theta(\omega) = H(\omega)\beta(\omega)$ (note that, for stress and strain, the transfer function is equal to the complex shear modulus G*). Making the assumption that β is linearly proportional to the voltage applied to the electromagnet, V(t), the ratio of Fourier transforms of θ to V yields the frequency dependent amplitude and phase of the bead:

$$\begin{aligned}
\theta(\omega) &= H(\omega)\beta(\omega) \\
&= \frac{\mathscr{F}[\theta(t)]}{\mathscr{F}[\beta(t)]}\beta(\omega) \\
&= \frac{\mathscr{F}[\theta(t)]}{\mathscr{F}[V(t)/|V|]}\frac{\beta(\omega)}{\beta_0} \\
\frac{\beta_0}{\beta(\omega)}\theta(\omega) &= \frac{\mathscr{F}[\theta(t)]}{\mathscr{F}[V(t)/|V|]} \\
\theta_0(\omega)\exp[i\phi] &= \frac{\mathscr{F}[\theta(t)]}{\mathscr{F}[V(t)/|V|]}
\end{aligned} \tag{5.3}$$

where the previous definitions of $\beta(t)$ and $\theta(t)$ have been used and $\mathscr{F}[\,]$ denotes the Fourier transform operator. By simultaneously capturing the motion of the particle and the voltage driving the magnetic field, the frequency response can be calculated,

as shown in Figure 5.4b-f, where the amplitude is fit to Equation 5.1 in order to obtain ω^*, and hence the fluid viscosity.

5.2. A Newtonian Fluid

In order to extract the viscosity η from the fit parameter $\omega^* \equiv mB/\xi\eta$, it is first necessary to determine the unknown system parameters m and ξ, which are properties of the probe particles, and B, which is determined by the static magnetic field and driving voltage on the electromagnet. Because of the uniformity of the magnetic particles, this requirement can be relaxed to knowing the quantity mB/ξ at a particular driving voltage that is used for all experiments (as evidenced in Figure 5.4a), or this quantity's voltage dependence in the case where one wants to measure effects such as shear thinning. This can easily be accomplished by measuring the frequency response in a substance of known viscosity (independently measured via passive microrheology), which was performed in water/glycerol solutions and is summarized in Figure 5.4.

Thermal diffusion of colloidal particles was used in conjunction with the Stokes-Einstein relation in order to independently measure the viscosity of the water/glycerol solution used to calibrate the experiment. First, fluorescent micro-spheres with a diameter of 1 μm (Spherotech) where suspended in 85% glycerol and placed into the light sheet microscope. The Brownian motion of these particles was captured at 100 frames per second and the images were loaded into a particle tracking software package developed in our lab [93, 94], which returns the position of the particle with sub-pixel resolution as a function of time. From these tracks, the mean squared displacement is calculated and used to find the diffusion coefficient $\mathcal{D}$ via the relation $\left\langle (r)^2 \right\rangle = 4\mathcal{D}t$, where r is the two-dimensional displacement, t is time, and $\langle\ \rangle$ indicates averaging over all walks of length t. Knowing $\mathcal{D}$, viscosity can be calculated via the Stokes-Einstein

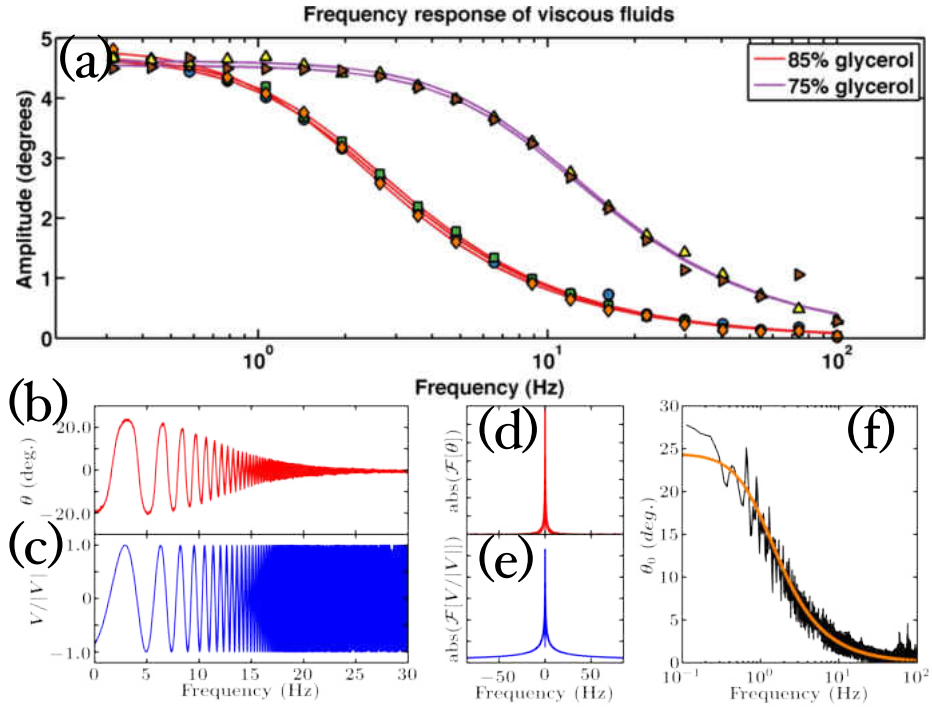

FIGURE 5.4. Frequency response in a Newtonian fluid (glycerol). (a) Sequentially measured frequency response of magnetic particle in 75% (N=2) and 85% glycerol. Symbols are data points and curves are fits to Equation 5.1. (b-f) Chirped frequency response of particle in 85% glycerol. (b) and (c) show the measured orientation of the particle and the normalized voltage applied to the electromagnet. (d) and (e) show the spectrums of (b) and (c), which are used in 5.3 to calculate $\theta_0(\omega)$ (f, black), which can be fit to Equation 5.1 (f, orange).

relation:

$$\mathcal{D} = \frac{k_B T}{6\pi\eta a} \tag{5.4}$$

where k_B is Boltzmann's constant, T is temperature, and a is the radius of the particle. Using this method, I measure the viscosity of the calibration sample (≈85 % glycerol by weight) to be 49.7 cP, consistent with tabulated values, which are very sensitive to composition in this concentration regime.

5.3. Perivitelline Fluid

Applying this method to biological samples can be accomplished quite readily, here I demonstrate its use to perform what are, to the best of my knowledge, the first measurements of the fluid that occupies the periviteline space of zebrafish embryos. As shown in Figure 1.1a, the zebrafish embryo is separated from the external environment by a thin membrane called the chorion. This structure, along with the fluid that is contained between it and the embryo, has long history of microscopic study. Hisaoka (1958) showed that it is a leaky membrane covered with 1.5 μm holes and therefore permeable to water and electrolytes. In his study, he also noted the liquid within as "...a slightly opalescent fluid. The viscous nature of this fluid may be readily observed as it comes in contact with water when the chorion is ruptured by means of dissecting needles" [95].

While it is very common to de-chorionate zebrafish embryos and then place them in weak gels to facilitate the microscopic study of development, it has recently been shown that the viscosity of the fluid or gel in which they are embedded during imaging can have significant effects on morphological development [96]. It is therefore worthwhile to determine the fluid properties in the natural developmental state by measuring the viscosity of the periviteline fluid *in vivo*. To do this, I injected several

chorions (N = 10) with 5 nL of elongated magnetic particles suspended in embryo medium (Drummond NanoJect II micro-injector). Since the total volume of the periviteline space is approximately 0.5 μL, the introduction of tracer particles with embryo medium constitutes only a 1% change in the composition of the fluid. Before imaging, the embryos were allowed to rest for two hours in order to give the embyro medium a chance to thoroughly mix into the periviteline fluid, which was confirmed by observing the fluorescent tracer particles had evenly distributed throughout the periviteline space. The frequency response was measured for beads in each of the ten samples and fit to equation Equation 5.1 in order to obtain values for the fluid viscosity, which was found to have a value of 2.64 $\pm$ 0.19 cP (given as mean $\pm$ one standard deviation of the mean), or 2.64 times that of water (Figure 5.5).

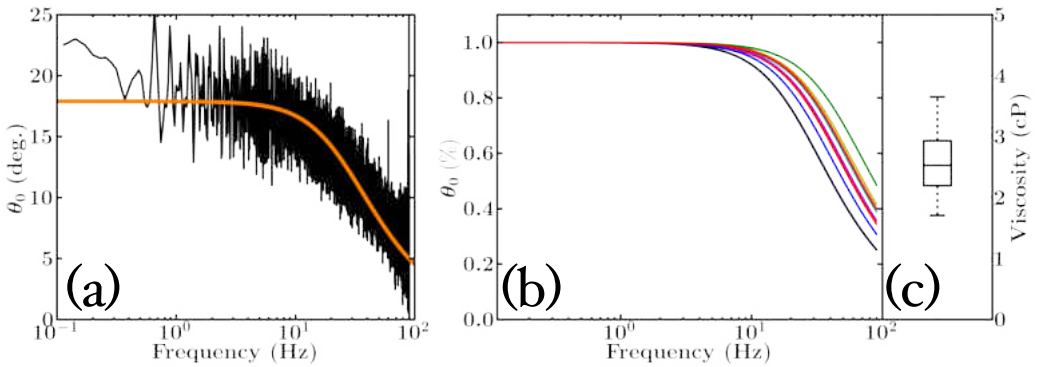

FIGURE 5.5. Frequency response of magnetic particle in the periviteline space. (a) Data and fit to Equation 5.1 for one representative data set. (b) Fits to Equation 5.1 for all samples (N=10). (c) Distribution of values for viscosity. Midline represents the median value, the box extends from the first to third quartile (containing 50% of the data), and the whiskers extend to the highest and lowest data points.

5.4. Material Properties of Intestinal Mucus in Larval Zebrafish

Chapter IV discussed the importance of colonizing bacteria for the health of an animal and that the majority of these bacteria live in the gastrointestinal system.

In order to understand how species of bacteria efficiently colonize and maintain a stable population within the gut, it would be useful to study some of the properties of this environment, namely, the fluid properties of the mucus in which bacteria reside. Intestinal mucus is known to play a role in controlling bacterial infection in the healthy human gut [97] and a number of studies have probed its material properties [85, 87, 98]. Because of the difficulty in obtaining sufficient quantities of uncontaminated samples, previous studies have mainly been performed on an *in vitro* model, such as reconstituted porcine gastric mucus. These studies have often found a dependence of the measured viscosity on the pH of the sample, indicating that an unperturbed sample would be preferred, since pH is highly variable *in vivo*. Furthermore, when comparing values measured on different scales, Celli *et al* found a 100-fold difference in the microscale and macroscale viscosities of porcine gastric mucus [98]. For these reasons, I performed an *in vivo* measurement of intestinal mucus on the microscale using the magnetic microrheology technique described above.

5.4.1. Micro-gavage of Zebrafish Lavae

As a prerequisite to performing a microrheological measurement *in vivo*, tracer particles must be introduced into the system. This could, in principle be done by doping a food source with the magnetic particles prior to feeding the zebrafish larvae. Such a strategy would, however, change the gut environment substantially by the introduction of food matter. Furthermore, we would like to be able to preserve the germ-free or gnotobiotic nature of specimens in order to address physiological questions where the properties of the mucus may change. Probe particles could be introduced into the fish's water, with a chance that some will be ingested, either intentionally or unintentionally. This strategy was attempted, but resulted in a

disappointing rate of success. I therefore adopted a recently developed technique of orally gavaging zebrafish larvae [99], where fluid is delivered to the intestinal bulb by inserting a micro-pipette tip down the esophagus of the fish and injecting a small volume of material (see Figure 5.6).

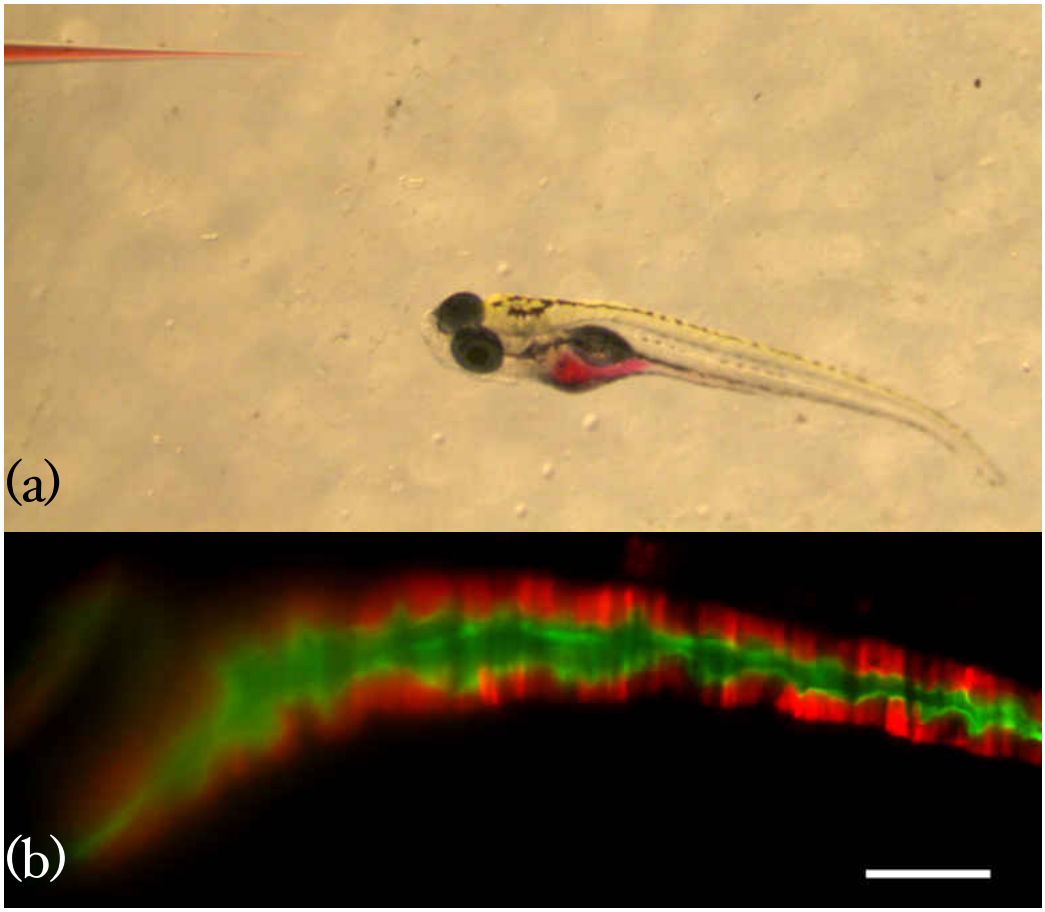

FIGURE 5.6. (a) Zebrafish larva gavaged with phenol red to illustrate gut lumen. The gavage needle is shown in the upper left corner. (b) Fluorescence image showing the gut lumen (red) immediately posterior to the bulb, recently gavaged with wheat germ agglutinin (green), which binds to the intestinal mucus. Scale bar is 50 microns.

Five day post fertilization fish were anesthetized with tricane and placed into 4% methylcellulose on a plate of stiff agarose gel. Borosilicate glass capillaries were pulled to a diameter of $\varnothing \approx 30\ \mu$m, made hydrophilic by treating in a 30% oxygen plasma

cleaner, and loaded onto the micro-injector with micropositioning system. Magnetic probe particles suspended in embryo medium were then loaded into the capillary and microgavaged as described in [99]. Fish were then allowed to recover for a period of at least two hours before imaging commences, in order to allow the internal environment of the intestinal bulb to equilibrate and return to pre-gavage composition.

In order to ensure that the luminal contents returned to a pre-gavage composition before performing measurements, a number of fish were first gavaged with fluorescent dextran and immediately mounted in the light sheet microscope. Gut contents were imaged once every ten minutes for several hours and the fluorescence level at each time point was used as a measure of what percentage of gavage-delivered fluid remained. We observed this to decrease to background levels in approximately two hours, as shown in Figure 5.7.

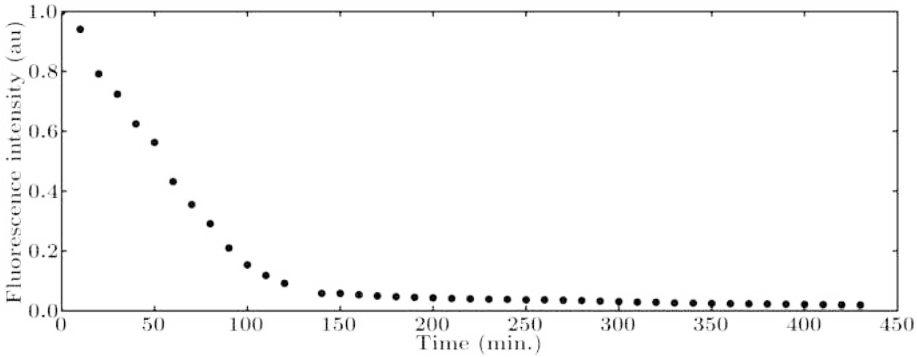

FIGURE 5.7. Gut composition post gavage: Fluorescent dextran solution was gavaged into a 5 dpf zebrafish larva, which was then mounted in the light sheet microscope and imaged every ten minutes. The fluorescence intensity decreases roughly linearly, becoming indistinguishable from the background at around two hours post gavage.

5.4.2. Results

Zebrafish larvae (5 dpf) were orally gavaged, as described above, with fluorescent magnetic tracer particles (original diameter $\approx 4.8\,\mu$m) and allowed to recover for at least

two hours prior to imaging. Restricting the data to beads that remained in the intestinal bulb after this recovery period, I obtained measurements from several fish (N = 16) that had magnetic particles which were multiple bead-lengths away from the boundary of the gut (in order to avoid the wall's effect on the bead). Once anesthetized and mounted on the light sheet microscope, these particles were submitted to an oscillating magnetic field as described above The results are summarized in Figure 5.8. Interestingly, I again find that the material response is consistent with Equation 5.1, despite the viscoelastic nature of mucus derived from other systems [85, 87, 98]. The results of fitting to Equation 5.1 yield a value for the viscosity of mucus within the zebrafish intestinal bulb of 5.40 ± 0.54 cP (given as the mean ± the standard deviation of the mean). It is also

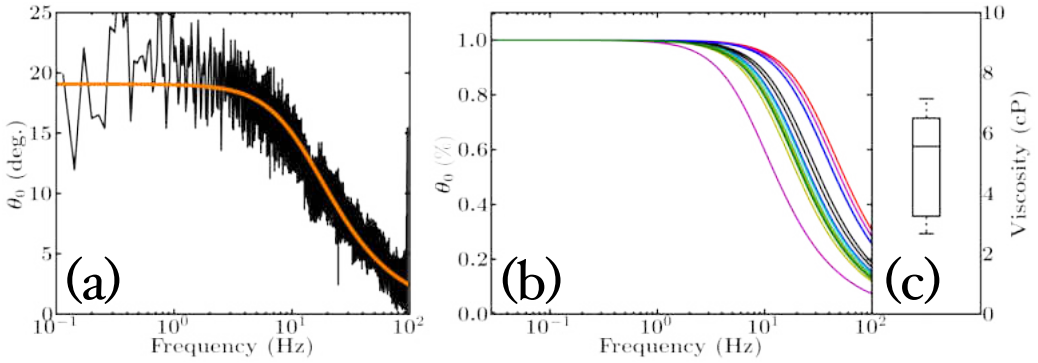

FIGURE 5.8. Frequency response of magnetic particle in the intestinal bulb of a 5 dpf zebrafish larva. (a) Data and fit to Equation 5.1 for one representative data set. (b) Fits to Equation 5.1 for all samples (N=16). (c) Distribution of values for viscosity. Midline represents the median value, the box extends from the first to third quartile (containing 50% of the data), and the whiskers extend to the highest and lowest data points.

beneficial to consider what type of elastic component may be present and place bounds on its magnitude that are consistent with the data. To do this, I consider the Maxwell model of a viscoelastic fluid, characterized by a single relaxation time [100]. While very few materials exactly follow this model, it is a good first order approximation in our case because the relaxation time will simply appear as the largest component of

the distribution of relaxation times of a generalized model. Solving the constitutive equation for a Maxwell fluid yields the analog of Equation 5.1:

$$\theta_0 = \beta_0 \sqrt{\frac{1 + (\omega\tau)^2}{1 + (\omega\tau)^2 \left(1 + C/mB\right)^2}} \tag{5.5}$$

where, in this case $\tau \equiv \eta/G$, G is the elastic modulus, and $C \equiv \zeta G$ is the elastic modulus multiplied by the appropriate geometrical constant. Fitting the data to this model, assuming the previously obtained values of viscosity to still be valid, suggests an elastic modulus no greater than ≈ 1 Pascal, in agreement with previously published microrheological measurements *in vitro* in porcine gastric mucus [98].

5.5. Discussion

Here I have established a practical method for measuring the viscosity of biological fluids *in vivo*, using the minimally invasive tools of fluorescence microscopy and magnetic fields. Using this method, I have given the first such measurements on two biological fluids that have important effects on development. The viscosity of mucus in the zebrafish larval gut was found to be surprisingly low and lacking a significant elastic component, in contrast with bulk measurements made on similar substances *in vitro*. These facts motivate the extension of measurements to more fully characterize the basic material properties of mucus at the length scale of microns. For example, the non-newtonian behavior of shear-thinning could be measured by varying the driving amplitude of the magnetic field and may be relevant to the proper function of peristalsis in the zebrafish gut. Additionally, and perhaps most importantly, this technique may be used to explore the variation in the intestinal environment in response to stimuli or across different phenotypes. Many biological questions may then be asked, for

example, does the intestinal mucus change in response to bacterial colonization? How would such a response depend on the constituent members of the bacterial community? Would such a change be mediated by the host or by the microbe? These are questions that can only be answered by a non-destructive, *in vivo* technique such as the one developed here.

As the importance of animals' microbiota becomes better understood, imaging-based techniques that can access the system over extended periods of time and with cellular spatial resolution have the opportunity to significantly augment the knowledge obtained from system-level techniques such as genomic sequencing. It is my hope that the methods developed here can have an impact on what is known in these systems and help to facilitate future techniques and instrumentation.

REFERENCES CITED

[1] Philip Nelson. *Biological Physics*. W. H. Freeman & Company, New York, 2004.

[2] Rob Phillips, Jane Kondev, Julie Theriot, and Hernan G Garcia. *Physical Biology of the Cell*. Garland Science, 2012.

[3] S Block, L Goldstein, and B Schnapp. Bead movement by single kinesin molecules studied with optical tweezers. *Nature*, Jan 1990.

[4] J Liphardt, B Onoa, S Smith, I Tinoco, and C Bustamante. Reversible unfolding of single rna molecules by mechanical force. *Science*, Jan 2001.

[5] D Fung and H Berg. Powering the flagellar motor of escherichia coli with an external voltage source. *Nature*, Jan 1995.

[6] Mathias Köppen, Beatriz Fernández, Lara Carvalho, Antonio Jacinto, and Carl-Philipp Heisenberg. Coordinated cell-shape changes control epithelial movement in zebrafish and drosophila. *Development*, 133(14):2671–2681, 2006.

[7] Philipp J Keller, Annette D Schmidt, Joachim Wittbrodt, and Ernst H. K Stelzer. Reconstruction of zebrafish early embryonic development by scanned light sheet microscopy. *Science*, 322(5904):1065–1069, Jan 2008. doi: 10.1126/science.1162493.

[8] Guy B Blanchard, Alexandre J Kabla, Nora L Schultz, Lucy C Butler, Benedicte Sanson, Nicole Gorfinkiel, L Mahadevan, and Richard J Adams. Tissue tectonics: morphogenetic strain rates, cell shape change and intercalation. *Nature Methods*, 6(6):458–464, Jan 2009. doi: 10.1038/nmeth.1327.

[9] B Schmid, G Shah, N Scherf, and M Weber.... High-speed panoramic light-sheet microscopy reveals global endodermal cell dynamics. *Nature*, Jan 2013.

[10] Paul Scherz, Jan Huisken, Pankaj Sahai-Hernandez, and Didier Stainier. High-speed imaging of developing heart valves reveals interplay of morphogenesis and function. *Development*, 135(6):1179–1187, 2008.

[11] Aristides Arrenberg, Didier Stainier, Herwig Baier, and Jan Huisken. Optogenetic control of cardiac function. *Science*, 330(6006):971–974, 2010.

[12] J Taylor, J Girkin, and G Love. High-resolution 3d optical microscopy inside the beating zebrafish heart using prospective optical gating. *Biomedical optics express*, Jan 2012.

[13] Dominic Wells. Assessing the welfare of genetically altered mice: Full report of ga mouse welfare working group. *The National Centre for the Replacement, Refinement and Reduction of Animals in Research (NC3Rs)*, 2006.

[14] DJ Grunwald and JS Eisen. Headwaters of the zebrafish—emergence of a new model vertebrate. *Nat Rev Genet.*, 3(9):717–724, 2002.

[15] Charles Kimmel, William Ballard, Seth Kimmel, Bonnie Ullmann, and Thomas Schilling. Stages of embryonic development of the zebrafish. *Dev Dynam.*, 203(3): 253–310, 1995.

[16] Y Pan, Tom Freundlich, Tamily Weissman, David Schoppik, X Wang, Steve Zimmerman, Brian Ciruna, Joshua Sanes, Jeff Lichtman, and Alexander Schier. Zebrabow: multispectral cell labeling for cell tracing and lineage analysis in zebrafish. *Development.*, 140(13):2835–2846, 2013.

[17] Linh Pham, Michelle Kanther, Ivana Semova, and John Rawls. Methods for generating and colonizing gnotobiotic zebrafish. *Nature Protocols*, 3(12):1862–1875, 2008.

[18] Kathryn Milligan-Myhre, Jeremy Charette, Ryan Phennicie, W Stephens, John Rawls, Karen Guillemin, and Carol Kim. Study of host-microbe interactions in zebrafish. *Methods Cell Biol*, 105:87–116, 2011.

[19] C Canaria and R Lansford. Advanced optical imaging in living embryos. *Cellular and molecular life sciences*, Jan 2010.

[20] S Megason and S Fraser. Digitizing life at the level of the cell: high-performance laser-scanning microscopy and image analysis for in toto imaging of development. *Mechanisms of Development.*, Jan 2003.

[21] Mats G. L Gustafsson, Lin Shao, Peter M Carlton, C. J. Rachel Wang, Inna N Golubovskaya, W. Zacheus Cande, David A Agard, and John W Sedat. Three-dimensional resolution doubling in wide-field fluorescence microscopy by structured illumination. *Biophysical Journal*, 94(12):4957–4970, Jan 2008. doi: 10.1529/biophysj.107.120345.

[22] Lothar Schermelleh, Rainer Heintzmann, and Heinrich Leonhardt. A guide to super-resolution fluorescence microscopy. *The Journal of Cell Biology*, 190(2): 165–175, 2010.

[23] Thai V Truong, Willy Supatto, David S Koos, John M Choi, and Scott E Fraser. Deep and fast live imaging with two-photon scanned light-sheet microscopy. *Nature Methods*, Jul 2011. doi: doi:10.1038/nmeth.1652.

[24] Tobias Breuninger, Klaus Greger, and Ernst H. K Stelzer. Lateral modulation boosts image quality in single plane illumination fluorescence microscopy. *Opt. Lett.*, 32(13):1938–1940, Jan 2007.

[25] Philipp J Keller, Annette D Schmidt, Anthony Santella, Khaled Khairy, Zhirong Bao, Joachim Wittbrodt, and Ernst H. K Stelzer. Fast, high-contrast imaging of animal development with scanned light sheet-based structured-illumination microscopy. *Nature Methods*, 7(8):637–U55, Jan 2010. doi: 10.1038/NMETH.1476.

[26] T Planchon, L Gao, D Milkie, and M Davidson.... Rapid three-dimensional isotropic imaging of living cells using bessel beam plane illumination. *Nature Methods*, Jan 2011.

[27] Douglas B. Murphy. *Fundamentals of light microscopy and electronic imaging*. Wiley-Liss, Inc., 2001.

[28] M Westerfield. The zebrafish book: a guide for the laboratory use of zebrafish (brachydanio rerio). *The zebrafish book: a guide for the laboratory use of zebrafish (Brachydanio rerio)*, Jan 1993.

[29] Raju Tomer, Khaled Khairy, Fernando Amat, and Philipp J Keller. Quantitative high-speed imaging of entire developing embryos with simultaneous multiview light-sheet microscopy. *Nature Methods*, pages 1–14, Mar 2012. doi: 10.1038/nmeth.2062.

[30] K Greger, J Swoger, and E. H. K Stelzer. Basic building units and properties of a fluorescence single plane illumination microscope. *Rev. Sci. Instrum.*, 78(2):023705, Jan 2007. doi: 10.1063/1.2428277.

[31] Peter Santi. Light sheet fluorescence microscopy a review. *Journal of Histochemistry & Cytochemistry*, 59(2):129–138, 2011.

[32] Jan Huisken and Didier Y. R Stainier. Selective plane illumination microscopy techniques in developmental biology. *Development*, 136(12):1963–1975, Jan 2009. doi: 10.1242/dev.022426.

[33] Liang Gao, Lin Shao, Christopher D Higgins, John S Poulton, Mark Peifer, Michael W Davidson, Xufeng Wu, Bob Goldstein, and Eric Betzig. Noninvasive imaging beyond the diffraction limit of 3d dynamics in thickly fluorescent specimens. *Cell*, 151(6):1370–1385, Dec 2012. doi: 10.1016/j.cell.2012.10.008.

[34] Peter M Carlton, Jerome Boulanger, Charles Kervrann, Jean-Baptiste Sibarita, Jean Salamero, Susannah Gordon-Messer, Debra Bressan, James E Haber, Sebastian Haase, Lin Shao, Lukman Winoto, Atsushi Matsuda, Peter Kner, Satoru Uzawa, Mats Gustafsson, Zvi Kam, David A Agard, and John W Sedat. Fast live simultaneous multiwavelength four-dimensional optical microscopy. *Proc. Natl. Acad. Sci.*, 107(37):16016–16022, Jan 2010. doi: 10.1073/Proc. Natl. Acad. Sci..1004037107.

[35] April DeLaurier, B. Frank Eames, Bernardo Blanco-Sanchez, Gang Peng, Xinjun He, Mary E Swartz, Bonnie Ullmann, Monte Westerfield, and Charles B Kimmel. Zebrafish sp7:egfp: A transgenic for studying otic vesicle formation, skeletogenesis, and bone regeneration. *Genesis*, 48(8):505–511, Jan 2010. doi: 10.1002/dvg.20639.

[36] Charles B Kimmel, April DeLaurier, Bonnie Ullmann, John Dowd, and Marcie McFadden. Modes of developmental outgrowth and shaping of a craniofacial bone in zebrafish. *Plos One*, 5(3):e9475, Jan 2010. doi: 10.1371/journal.pone.0009475.

[37] N Li, K Felber, P Elks, and P Croucher.... Tracking gene expression during zebrafish osteoblast differentiation. *Developmental Dynamics*, Jan 2009.

[38] C Cubbage and P Mabee. Development of the cranium and paired fins in the zebrafish danio rerio (ostariophysi, cyprinidae). *J Morphol*, Jan 1996.

[39] Fishface: An atlas of zebrafish craniofacial development, 2012. URL `https://www.facebase.org/fishface/home`.

[40] Philipp J Keller and Ernst H. K Stelzer. Quantitative in vivo imaging of entire embryos with digital scanned laser light sheet fluorescence microscopy. *Curr Opin Neurobiol*, 18(6):624–632, Jan 2008. doi: 10.1016/j.conb.2009.03.008.

[41] J.B Pawley. *Handbook of Biological Confocal Microscopy*. Springer, 2006.

[42] Ralph Gräf, Jens Rietdorf, and Timo Zimmermann. Live cell spinning disk microscopy. In Jens Rietdorf, editor, *Microscopy Techniques*, volume 95 of *Advances in Biochemical Engineering*, pages 57–75. Springer Berlin Heidelberg, 2005. ISBN 978-3-540-23698-6. doi: 10.1007/b102210. URL `http://dx.doi.org/10.1007/b102210`.

[43] C. Solomon and T. Breckon. *Fundamentals of Digital Image Processing: A Practical Approach with Examples in Matlab*. John Wiley and Sons, 2011.

[44] Matthew Jemielita, Michael J Taormina, April DeLaurier, Charles B Kimmel, and Raghuveer Parthasarathy. Comparing phototoxicity during the development of a zebrafish craniofacial bone using confocal and light sheet fluorescence microscopy techniques. *Journal of Biophotonics*, 6(11-12):920–928, Dec 2012. doi: 10.1002/jbio.201200144.

[45] C.B. Kimmel, C.T. Miller, G. Kruze, B. Ullmann, R.A. BreMiller, K.D. Larison, and H.C. Snyder. The shaping of pharyngeal cartilages during early development of the zebrafish. *Developmental Biology*, 203:245–263, 1998.

[46] L. Dethlefsen, M. McFall-Ngai, and D. A. Relman. An ecological and evolutionary perspective on human-microbe mutualism and disease. *Nature*, 449 (7164):811–818, Oct 2007.

[47] A. Spor, O. Koren, and R. Ley. Unravelling the effects of the environment and host genotype on the gut microbiome. *Nat. Rev. Microbiol.*, 9(4):279–290, Apr 2011.

[48] J. Kuczynski, C. L. Lauber, W. A. Walters, L. W. Parfrey, J. C. Clemente, D. Gevers, and R. Knight. Experimental and analytical tools for studying the human microbiome. *Nature Reviews Genetics*, 13:47–58, January 2012.

[49] S. V. Nyholm and M. J. McFall-Ngai. The winnowing: establishing the squid-vibrio symbiosis. *Nat. Rev. Microbiol.*, 2(8):632–642, Aug 2004.

[50] S. V. Nyholm, E. V. Stabb, E. G. Ruby, and M. J. McFall-Ngai. Establishment of an animal-bacterial association: recruiting symbiotic vibrios from the environment. *Proc. Natl. Acad. Sci. U.S.A.*, 97(18):10231–10235, Aug 2000.

[51] S. V. Nyholm, B. Deplancke, H. R. Gaskins, M. A. Apicella, and M. J. McFall-Ngai. Roles of Vibrio fischeri and nonsymbiotic bacteria in the dynamics of mucus secretion during symbiont colonization of the Euprymna scolopes light organ. *Appl. Environ. Microbiol.*, 68(10):5113–5122, Oct 2002.

[52] K. J. Boettcher, E. G. Ruby, and M. J. McFall-Ngai. Bioluminescence in the symbiotic squid *Euprymna scolopes* is controlled by a daily biological rythym. *Proc. Natl. Acad. Sci.*, 179:65–73, 1996.

[53] G. T. Macfarlane, S. Macfarlane, and G. R. Gibson. Validation of a Three-Stage Compound Continuous Culture System for Investigating the Effect of Retention Time on the Ecology and Metabolism of Bacteria in the Human Colon. *Microb. Ecol.*, 35(2):180–187, Mar 1998.

[54] S. E. Cheesman and K. Guillemin. We know you are in there: conversing with the indigenous gut microbiota. *Res. Microbiol.*, 158(1):2–9, 2007.

[55] M. Kanther and J. F. Rawls. Host-microbe interactions in the developing zebrafish. *Curr. Opin. Immunol.*, 22(1):10–19, Feb 2010.

[56] Jennifer M Bates, Erika Mittge, Julie Kuhlman, Katrina N Baden, Sarah E Cheesman, and Karen Guillemin. Distinct signals from the microbiota promote different aspects of zebrafish gut differentiation. *Dev Biol*, 297(2):374–386, Jan 2006. doi: 10.1016/j.ydbio.2006.05.006.

[57] J. M. Bates, J. Akerlund, E. Mittge, and K. Guillemin. Intestinal alkaline phosphatase detoxifies lipopolysaccharide and prevents inflammation in zebrafish in response to the gut microbiota. *Cell Host Microbe*, 2(6):371–382, Dec 2007.

[58] S. E. Cheesman, J. T. Neal, E. Mittge, B. M. Seredick, and K. Guillemin. Epithelial cell proliferation in the developing zebrafish intestine is regulated by the Wnt pathway and microbial signaling via Myd88. *Proc. Natl. Acad. Sci. U.S.A.*, 108 Suppl 1:4570–4577, Mar 2011.

[59] J. F. Rawls, M. A. Mahowald, R. E. Ley, and J. I. Gordon. Reciprocal gut microbiota transplants from zebrafish and mice to germ-free recipients reveal host habitat selection. *Cell*, 127(2):423–433, Oct 2006.

[60] G. Roeselers, E. K. Mittge, W. Z. Stephens, D. M. Parichy, C. M. Cavanaugh, K. Guillemin, and J. F. Rawls. Evidence for a core gut microbiota in the zebrafish. *ISME J*, 5(10):1595–1608, Oct 2011.

[61] J. M. Davis and L. Ramakrishnan. The role of the granuloma in expansion and dissemination of early tuberculous infection. *Cell*, 136(1):37–49, Jan 2009.

[62] J. F. Rawls, M. A. Mahowald, A. L. Goodman, C. M. Trent, and J. I. Gordon. In vivo imaging and genetic analysis link bacterial motility and symbiosis in the zebrafish gut. *Proc. Natl. Acad. Sci. U.S.A.*, 104(18):7622–7627, May 2007.

[63] S. A. Renshaw, C. A. Loynes, D. M. Trushell, S. Elworthy, P. W. Ingham, and M. K. Whyte. A transgenic zebrafish model of neutrophilic inflammation. *Blood*, 108 (13):3976–3978, Dec 2006.

[64] A. N. Ng, T. A. de Jong-Curtain, D. J. Mawdsley, S. J. White, J. Shin, B. Appel, P. D. Dong, D. Y. Stainier, and J. K. Heath. Formation of the digestive system in zebrafish: III. Intestinal epithelium morphogenesis. *Dev. Biol.*, 286(1):114–135, Oct 2005.

[65] P. J. Rombough. Ontogenetic changes in the toxicity and efficacy of the anaesthetic MS222 (tricaine methanesulfonate) in zebrafish (Danio rerio) larvae. *Comp. Biochem. Physiol., Part A Mol. Integr. Physiol.*, 148(2):463–469, Oct 2007.

[66] J. L. Sonnenburg, L. T. Angenent, and J. I. Gordon. Getting a grip on things: how do communities of bacterial symbionts become established in our intestine? *Nat. Immunol.*, 5(6):569–573, Jun 2004.

[67] H. L. Smith and P. Waltman. *The theory of the Chemostat: dynamics of microbial competition*. Cambridge University Press, 1995.

[68] Michael J Taormina, Matthew Jemielita, W Stephens, Adam Burns, Joshua Troll, Raghuveer Parthasarathy, and Karen Guillemin. Investigating bacterial-animal symbioses with light sheet microscopy. *The Biological Bulletin*, 223(1):7–20, 2012.

[69] M. van der Marel, V. Schroers, H. Neuhaus, and D. Steinhagen. Chemotaxis towards, adhesion to, and growth in carp gut mucus of two Aeromonas hydrophila strains with different pathogenicity for common carp, Cyprinus carpio L. *J. Fish Dis.*, 31(5):321–330, May 2008.

[70] M. Altarriba, S. Merino, R. Gavin, R. Canals, A. Rabaan, J. G. Shaw, and J. M. Tomas. A polar flagella operon (flg) of Aeromonas hydrophila contains genes required for lateral flagella expression. *Microb. Pathog.*, 34(5):249–259, May 2003.

[71] Y. Feng, C. Santoriello, M. Mione, A. Hurlstone, and P. Martin. Live imaging of innate immune cell sensing of transformed cells in zebrafish larvae: parallels between tumor initiation and wound inflammation. *PLoS Biol.*, 8(12):e1000562, 2010.

[72] S. K. Yoo, Q. Deng, P. J. Cavnar, Y. I. Wu, K. M. Hahn, and A. Huttenlocher. Differential regulation of protrusion and polarity by PI3K during neutrophil motility in live zebrafish. *Dev. Cell*, 18(2):226–236, Feb 2010.

[73] E. Colucci-Guyon, J. Y. Tinevez, S. A. Renshaw, and P. Herbomel. Strategies of professional phagocytes in vivo: unlike macrophages, neutrophils engulf only surface-associated microbes. *J. Cell. Sci.*, 124(Pt 18):3053–3059, Sep 2011.

[74] R. C. Gonzalez and R. E. Woods. *Digital image procssing*. Addson-Wesley, 1992.

[75] E. Borenstein, M. Kupiec, M. W. Feldman, and E. Ruppin. Large-scale reconstruction and phylogenetic analysis of metabolic environments. *Proc. Natl. Acad. Sci. U.S.A.*, 105(38):14482–14487, Sep 2008.

[76] S. Greenblum, P. J. Turnbaugh, and E. Borenstein. Metagenomic systems biology of the human gut microbiome reveals topological shifts associated with obesity and inflammatory bowel disease. *Proc. Natl. Acad. Sci. U.S.A.*, 109(2):594–599, Jan 2012.

[77] J. L. Green, B. J. Bohannan, and R. J. Whitaker. Microbial biogeography: from taxonomy to traits. *Science*, 320(5879):1039–1043, May 2008.

[78] C. Huffaker. Experimental studies of predation: dispersion factors and predator-prey oscillations. *Hilgardia*, 21:795–835, 1958.

[79] N. Fierer, D. Nemergut, R. Knight, and J. M. Craine. Changes through time: integrating microorganisms into the study of succession. *Res. Microbiol.*, 161(8): 635–642, Oct 2010.

[80] O. N. Bjørnstad, R. A. Ims, and X. Lambin. Spatial population dynamics: analyzing patterns and processes of population synchrony. *Trends Ecol. Evol. (Amst.)*, 14(11):427–432, Nov 1999.

[81] R. E. Ley, C. A. Lozupone, M. Hamady, R. Knight, and J. I. Gordon. Worlds within worlds: evolution of the vertebrate gut microbiota. *Nat. Rev. Microbiol.*, 6 (10):776–788, Oct 2008.

[82] Kenny Breuer, editor. *Microscale diagnostic techniques*, chapter 1: Microrheology. Springer, 2005.

[83] C Wilhelm, J Browaeys, A Ponton, and JC Bacri. Rotational magnetic particles microrheology: The maxwellian case. *Phys Rev E*, 67(1):011504, Jan 2003. doi: 10.1103/PhysRevE.67.011504.

[84] James S Bennett, Lachlan J Gibson, Rory M Kelly, Emmanuel Brousse, Bastian Baudisch, Daryl Preece, Timo A Nieminen, Timothy Nicholson, Norman R Heckenberg, and Halina Rubinsztein-Dunlop. Spatially-resolved rotational microrheology with an optically-trapped sphere. *Sci. Rep.*, 3:1–5, May 2013. doi: 10.1038/srep01759.

[85] Samuel K Lai, Ying-Ying Wang, Denis Wirtz, and Justin Hanes. Micro- and macrorheology of mucus. *Adv Drug Deliver Rev*, 61(2):86–100, Jan 2009. doi: 10.1016/j.addr.2008.09.012.

[86] National Institutes of Health. Human microbiome project, 2007-2015.

[87] Jonathan P Celli, Bradley S Turner, Nezam H Afdhal, Sarah Keates, Ionita Ghiran, Ciaran P Kelly, Randy H Ewoldt, Gareth H McKinley, Peter So, Shyamsunder Erramilli, and Rama Bansil. Helicobacter pylori moves through mucus by reducing mucin viscoelasticity. *Proc. Natl. Acad. Sci.*, 106(34):14321–14326, Jan 2009. doi: 10.1073/Proc. Natl. Acad. Sci..0903438106.

[88] J. A Champion, Y. K Katare, and S Mitragotri. From the cover: Making polymeric micro- and nanoparticles of complex shapes. *Proceedings of the National Academy of Sciences*, 104(29):11901–11904, Jul 2007. doi: 10.1073/Proc. Natl. Acad. Sci..0705326104.

[89] Oriol Guell, Francesc Sagues, and Pietro Tierno. Magnetically driven janus micro-ellipsoids realized via asymmetric gathering of the magnetic charge. *Adv Mater*, 23(32):3674–+, Jan 2011. doi: 10.1002/adma.201100902.

[90] G. Bradski. The OpenCV Library. *Dr. Dobb's Journal of Software Tools*, 2000.

[91] Eric Jones, Travis Oliphant, Pearu Peterson, et al. SciPy: Open source scientific tools for Python, 2001–.

[92] Leon Cohen. *Time-frequency Analysis: Theory and Applications*. Prentice Hall, 1994.

[93] Raghuveer Parthasarathy. Parthasarathy lab: Particle tracking, 2012–.

[94] Raghuveer Parthasarathy. Rapid, accurate particle tracking by calculation of radial symmetry centers. *Nature Methods*, 2012.

[95] Kenichi Hisaoka. Microscopic studies of the teleost chorion. *Transactions of the American Microscopical Society*, pages 240–243, 1958.

[96] A Kaufmann, M Mickoleit, M Weber, and J Huisken. Multilayer mounting enables long-term imaging of zebrafish development in a light sheet microscope. *Development*, 139(17):3242–3247, Sep 2012. doi: 10.1242/dev.082586.

[97] M. A. McGuckin, S. K. Lindén, P. Sutton, and T. H. Florin. Mucin dynamics and enteric pathogens. *Nature Reviews Microbiology*, 9:265–278, 2011.

[98] Jonathan Celli, Brian Gregor, Bradley Turner, Nezam Afdhal, Rama Bansil, and Shyamsunder Erramilli. Viscoelastic properties and dynamics of porcine gastric mucin. *Biomacromolecules*, 6(3):1329–1333, 2005.

[99] Jordan Cocchiaro and John Rawls. Microgavage of zebrafish larvae. *J Vis Exp*, 72 (e4434), Feb 2013.

[100] Patrick Oswald. *Rheophysics*. Cambridge University Press, 2009.